Review of Palaeobotany and Palynology 268 (2019) 1–18

Contents lists available at ScienceDirect

Review of Palaeobotany and Palynology

journal homepage: www.elsevier.com/locate/revpalbo

Controls on amorphous organic matter type and sulphurization in a Mississippian black shale

Joseph F. Emmings [a,b,*], Jan A.I. Hennissen [a], Michael H. Stephenson [a], Simon W. Poulton [c], Christopher H. Vane [a], Sarah J. Davies [b], Melanie J. Leng [d,e], Angela Lamb [d], Vicky Moss-Hayes [a]

[a] British Geological Survey, Keyworth, Nottingham NG12 5GG, UK
[b] School of Geography, Geology and the Environment, University of Leicester, Leicester LE1 7RH, UK
[c] School of Earth and Environment, University of Leeds, Leeds LS2 9JT, UK
[d] NERC Isotopes Geosciences Facilities, British Geological Survey, Keyworth, Nottingham NG12 5GG, UK
[e] Centre for Environmental Geochemistry, Sutton Bonington Campus, University of Nottingham, Sutton Bonington, Leicestershire LE12 5RD, UK

ARTICLE INFO

Article history:
Received 21 December 2018
Received in revised form 2 April 2019
Accepted 2 April 2019
Available online 5 April 2019

Keywords:
Mudstone
Amorphous organic matter
Sulphur
Redox

ABSTRACT

Paleoredox proxies (Fe speciation, trace element and $\delta^{34}S_{py}$) integrated with sedimentological and palynological observations link the distribution and type of particulate organic matter (OM) preserved to hydrocarbon source rock potential. In the Mississippian Bowland Shale Formation (Lancashire, UK), particulate OM is dominated by "heterogeneous" amorphous OM (AOM), primarily "sharp-edged, pellet-like" (AOMpel) and "heterogeneous, granular" (AOMgr) types. AOMpel is abundant in muds deposited under anoxic and moderately to highly sulphidic conditions and most likely represents the fecal minipellets of zooplankton and/or pellets of macrozooplankters. We recognize two intervals, "A" and "B," which exhibit $S_{org}/TOC > 0.04$, suggesting a bulk Type II-S kerogen composition. The Interval A palynofacies is typified by pyritized AOMpel (AOMpyr) particles that contain high-relief organic spheres surrounding individual pyrite framboids, within each AOMpyr particle. These textures are interpreted as sulphurized OM local to pyrite framboids ($S_{org\text{-}PF}$). $S_{org\text{-}PF}$ is rarely observed in Interval B, and absent in all other samples. Redox oscillation between ferruginous and euxinic conditions during early diagenesis of Interval A likely promoted S cycling in microenvironments surrounding pyrite framboids, which generated reactive S species and reactive OM required for sulphurization. Early diagenetic redox oscillation processes were apparently triggered by relative sea level fall, associated with an increased supply of Fe_{HR} from adjacent shelves into the basin. Interval B represents deposition during the late stages of basin infill and transition from anoxic to (sub)oxic bottom waters, where AOMpel is replaced by AOMgr as the dominant type of AOM. A large particle diameter at the limit of the mesh size (500 μm), sheet-like, fragmented character, and presence of candidate organic sheaths suggests AOMgr at least partially represent fragments of benthic microbial mats, probably as sulphide-oxidizers. A ternary plot of AOMpel + AOMpyr versus AOMgr versus spores + phytoclasts links the observed palynofacies to bottom and pore water redox conditions, water column productivity and proximity to fluvial (deltaic) supply of spores and phytoclasts. These variables were moderated by changing basin accommodation, driven primarily by eustatic sea level fluctuation. A sequence-stratigraphic control on AOM type and sulphurization is important for understanding the link between source rock heterogeneity and the timing of hydrocarbon generation and expulsion from this source rock.

1. Introduction

The upper unit of the Mississippian Bowland Shale Formation (Upper Bowland Shale; herein "Bowland Shale") is a potential target for unconventional hydrocarbon exploration and an important conventional hydrocarbon source rock in the UK (e.g., Andrews, 2013; Clarke et al., 2018) and time-equivalent units across Europe (Kerschke and Schulz, 2013; Nyhuis et al., 2015). The spatial and temporal distribution and type of organic matter (OM) in organic-rich mudstones, such as the Bowland Shale, is an important control on hydrocarbon prospectivity (e.g., Jarvie, 2012). Palynological assessment of particulate OM type yields important data relating to hydrocarbon source rock generative potential, particularly when supplemented with organic geochemical analyses such as RockEval pyrolysis (e.g., Espitalie et al., 1977). Palynofacies analysis can be used to quantify the proportions of highly aliphatic ("Type I"), moderately aliphatic ("Type II"), humic ("Type

* Corresponding author at: British Geological Survey, Keyworth, Nottingham NG12 5GG, UK.
E-mail address: josmin65@bgs.ac.uk (J.F. Emmings).

https://doi.org/10.1016/j.revpalbo.2019.04.004
0034-6667/

III") and refractory ("Type IV") palynofacies components (e.g., Tyson, 1995). Since sulphur (S) radicals associated with organic S (S_{org}) catalyze hydrocarbon maturation (Lewan, 1998), the recognition of S-rich (sulphurized) OM ("Type II-S") is also important with respect to understanding hydrocarbon source rock prospectivity (e.g., Orr, 1986; Dembicki, 2009).

In Mississippian organic-rich mudstones, in particular, the extracted palynological OM fraction (e.g., Wood et al., 1996) is dominated by amorphous OM (AOM; e.g., Könitzer et al., 2016; Hennissen et al., 2017). This is especially typical of Mississippian source rocks, given the lack of recognizable marine palynomorphs during the "Phytoplankton Blackout" (Pitrat, 1970; Riegel, 1996; Riegel, 2008; Servais et al., 2016; Tappan, 1970). This 100-Myr phenomenon is possibly explained by high nutrient availability, and therefore high rates of primary productivity, in the paleo-Rheic-Tethys seaway (Servais et al., 2016). These productive (low stress) conditions potentially supported phytoplankton which did not produce cysts, considered marine palynomorphs with relatively high preservation potential, because encystment was unnecessary (Servais et al., 2016).

AOM is usually described under transmitted and fluorescent light by eye (e.g., Tyson, 1995), and is often subdivided into "homogenous" and "heterogeneous" types (e.g., Hennissen et al., 2017). "Homogenous" AOM includes gellified humic material, and is therefore often interpreted as Type III OM (Tyson, 1995). "Heterogeneous" AOM is subdivided into "diffuse-edged" (also termed "granular") and "sharp-edged" AOM (Tyson, 1995). The former is typically interpreted as bacterial or highly degraded plant material and defined as Type III OM. "Sharp-edged" AOM is usually interpreted as "well-preserved" Type I or II OM, particularly if this is highly fluorescent under ultra-violet light (Tyson, 1995). Where AOM exhibits a distinctive orange color under transmitted light, this is usually a proxy for S-rich compounds (e.g., Tribovillard et al., 2001). Under suitable conditions, S may be incorporated into OM during syngenesis or early diagenesis, a process that is termed sulphurization (e.g., Sinninghe Damsté and De Leeuw, 1990a; Amrani, 2014).

In order to understand controls on the types and distribution of AOM and mechanisms for sulphurization, geochemical and palynological data were integrated through three sections of the Mississippian Upper Bowland Shale in the Craven Basin (Lancashire, UK), a basin with ongoing hydrocarbon exploration (Clarke et al., 2018). Palynofacies abundance data were integrated with syngenetic and early diagenetic paleoredox proxies including Fe-speciation, redox-sensitive trace element and $\delta^{34}S_{py}$ analyses.

2. Geological setting

The Bowland Shale was deposited in a series of epicontinental basins within the Rheic-paleo-Tethys paleoequatorial seaway, spanning from present-day North America to Poland (e.g., Davies et al., 1999). This seaway developed in response to oblique collision between Gondwana and Laurussia (Warr, 2000), including phases of extension (e.g., active rifting), thermal subsidence, strike-slip and compression tectonism. Mississippian extension (Leeder, 1982) generated a series of graben and half-graben structures, separated by platform "blocks" and "highs" (e.g., Waters and Davies, 2006) (Fig. 1a). Transition from active rifting to thermal subsidence broadly aligns with subdivision of the Bowland Shale Formation into lower and upper units coincident with the Visean-Serpukhovian boundary (Bisat, 1923; Davydov et al., 2012; Earp, 1961; Menning et al., 2006; Waters et al., 2009). The Upper Bowland Shale was deposited from the early to late Pendleian (~330–330.7 Ma; Gastaldo et al., 2009; Waters and Condon, 2012) in the Craven Basin (Fig. 1c).

The switch from rift to thermal sag, coupled with the advance of Pendle fluviodeltaic systems across and around the Askrigg Block, produced an interdigitating succession of hemipelagic and siliciclastic facies in the Craven Basin, as the mixed-to-siliciclastic Upper Bowland Shale (e.g., Brandon et al., 1998). Sedimentary facies include hemipelagites, turbidites, hybrid event beds and lenticular mudstones (Emmings et al., 2019) and the Hind Sandstone Member (Aitkenhead et al., 1992; Moseley, 1952; Moseley, 1962), which is an injectite (Kane, 2010). Craven Basin water depth likely ranged from ~100 to 200 m (Davies, 2008; Holdsworth and Collinson, 1988) through to several hundred metres (Davies et al., 1993).

Hemipelagic sediments in the Bowland Shale include discrete, macrofauna-bearing, calcareous sedimentary packages ("marine bands"; e.g., Ramsbottom, 1977; Fig. 1c) that are typically linked to starved siliciclastic input during the maximum rate of transgression (Posamentier et al., 1988) and/or at maximum marine flooding (Martinsen et al., 1995). Marine band cyclicity was likely a response to far-field ice-sheet volume on Gondwana (Veevers and Powell, 1987).

The macrofaunal body fossils present, particularly ammonoids, form the basis of a high-resolution biostratigraphic framework (Ramsbottom and Saunders, 1985). The ammonoid biozones E_{1a1}, E_{1b1}, E_{1b2} and E_{1c1} are recognized in the Upper Bowland Shale (e.g., Brandon et al., 1998) (Fig. 1c), with an average periodicity of 111 ka (Waters and Condon, 2012). Multiple flooding surfaces are recognized for E_{1a1} (a, b and c) and E_{1b2} (a and b) marine bands (Fig. 1c), which may represent sub-100 ka precession or obliquity forcing (Waters and Condon, 2012).

The Bowland Shale was followed by deposition of delta-top facies on the Askrigg Block and a submarine turbidite fan complex in the basin (Fraser and Gawthorpe, 1990; Kirby et al., 2000), as the Pendleton Formation (Waters et al., 2007) (Fig. 1c). Variscan inversion of the Craven Basin resulted in the development of a set of north-east south-west trending folds, thrust-folds and monoclines, collectively defined as the Ribblesdale Fold Belt (Arthurton, 1984; Gawthorpe, 1987) (Fig. 1b).

3. Materials and methods

Outcrop locality Hind Clough (grid ref.: 364430 453210, British National Grid projection) exposes the Upper Bowland Shale as a ~124 m thick stream-cut and weathered slope section (e.g., Moseley, 1962; Brandon et al., 1998; Emmings et al., 2019) on the north-west edge of the Ribblesdale Fold Belt (Arthurton, 1984; Gawthorpe, 1987). Together the sections at Hind Clough and in nearby boreholes Marl Hill 4 (MHD4; 367426 446752) and Cominco C9 (386010 463500) (Fig. 1b) were logged, sampled and assigned sedimentary facies (A–J) by Emmings et al. (2019). The stratigraphic framework was based on ammonoid biozones identified by Brandon et al. (1998). The sampling strategy was designed to minimize the potential for alteration due to modern weathering at outcrop, as implemented by Emmings et al. (2017).

3.1. Palynology

34 palynology samples were processed using standard preparation methods (Wood et al., 1996), using hydrochloric (36% vol/vol) and hydrofluoric (HF) (40% vol/vol) acid to remove carbonate and silicate phases, respectively. Kerogen residues were sieved at 500 and 10 μm. Residues were spiked with *Lycopodium clavatum* spores (batch no. 3862, MPA66949–66953, 2 tablets in 5 g sample; MPA67171–68150, 3 tablets in 5 g sample) in order to calculate absolute abundances using the marker grain method (Maher, 1981; Stockmarr, 1971). Since AOM was the primary target in this study, and highly abundant compared to spores, this precluded calculation of absolute abundances using the marker grain method. A much larger spike (i.e., >10 tablets) could potentially enable quantification of spore absolute abundances (but not AOM) in this material. A subset of residues were oxidized for 7 min using fuming nitric acid.

Each sample residue was strew-mounted onto two slides and set in low fluorescing Elvacite™ resin. Microscopic observations were conducted using an Axio Imager M2 m fitted with a motorized stage under transmitted light (brightfield and differential interference contrast) and incident green light. Green-light emission was attained

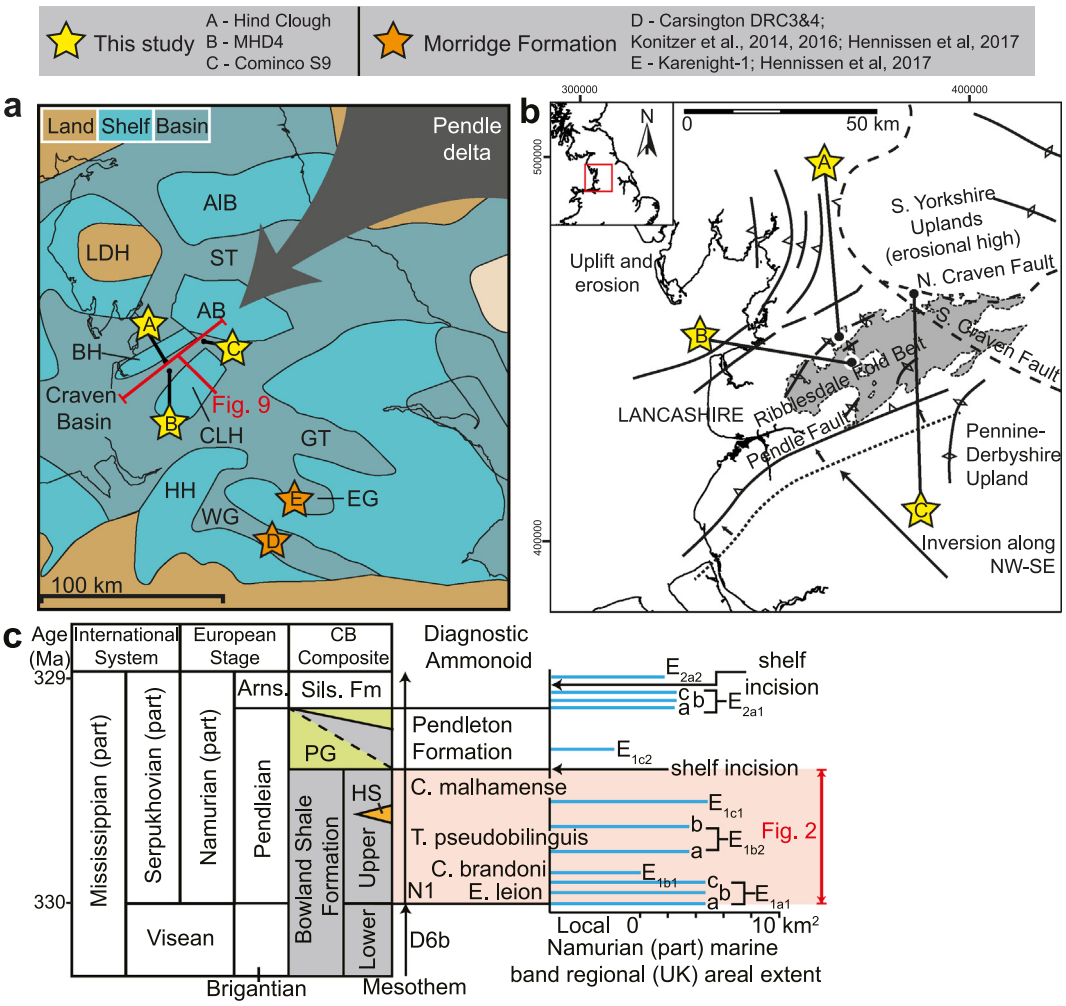

Fig. 1. (a) Regional basin structure modified from Waters et al. (2007), including the Craven Basin, study positions Hind Clough (A), MHD4 (B) and Cominco S9 (C), and UK coastline. Palynological studies by Hennissen et al. (2017) and Könitzer et al. (2016) through the broadly time equivalent (Pendleian to Arnsbergian) Morridge Formation from the Widmerpool Gulf (D) and Edale Gulf (E) are also plotted for reference. LDH = Lake District High; AlB = Alston Block; ST = Stainmore Trough; AB = Askrigg Block; BH = Bowland High; CLH = Central Lancashire High; GT = Gainsborough Trough; EG = Edale Gulf; WG = Widermerpool Gulf; HH = Holme High; (b) The Bowland Shale Formation is exposed as part of the Ribblesdale Fold Belt, including Westphalian structural elements (Fraser and Gawthorpe, 1990) and study sites Hind Clough (outcrop) and borehole Marl Hill 4 (MHD4). Outcrop extent data are based on DigMapGB-625, published with permission of the British Geological Survey. (c) Generalized Lower Namurian stratigraphy and Craven Basin composite after Brandon et al. (1998). Marine band areal extent data from Waters and Condon (2012), including diagnostic ammonoid fauna from Riley et al. (1993). Mesothems from Ramsbottom (1973). HS = Hind Sandstone Member. PG = Pendle Grit Member.

using a 100 V tungsten filament (HVP) lamp at maximum brightness passed through the Zeiss 00 Propidium Iodide (PI) filter set (λ 530–585 nm excitation). A subset of slides were also analyzed under a mercury HXP light source. Under green-light, the spectral irradiance for tungsten filament lamps and mercury lamps is similar (Lin and Davis, 1988). ×10, ×40 and ×100 (oil immersion) EC Plan Neofluor objectives were utilized. Emitted light was red-light filtered (530–585 nm λ beam-splitter, filtering emission above λ 615 nm).

Green light fluorescence (coupled with red light filter) was used as a proxy for moderately quenched (i.e., polymerized) structures and highly "delocalized" double bonds (Lin and Davis, 1988). Aromatic structures contain highly delocalized bonds, rather than acyclic compounds which may contain isolated double-bonds (e.g., alkenes, acyclic terpenoids). Thus green light fluorophors represent phenols and heteroatomic aromatic moieties contained within aliphatic polymers, and some aromatic (e.g., lignin-containing) substances. Highly polymerized substances that contain abundant delocalized bonds (e.g., humic compounds) promote quenching and are therefore typically non-fluorescent under all wavelengths (Lin and Davis, 1988).

Images were captured with an AxioCam MR R3 camera connected to a PC with Zen 2012 (Blue Edition) software. All images were captured in a dark room and under the same ambient light conditions. Particles were described and counted using an automatic stage, based on visual assessment and semi-automated analysis of extracted particle shape and fluorescence parameters using the Fiji ImageJ platform (Schindelin et al., 2012). Total AOM and AOMgr abundances are therefore relative and corrected for particle area. Palynofacies abundance data are provided in Appendix A.

3.2. Geochemistry

Samples selected for geochemical analysis were crushed and agate-milled to a fine powder. 193 samples were selected for pyrolysis, conducted on finely powdered samples in a Rock-Eval 6 pyrolyser (Vinci Technologies) in standard configuration and operated using the Bulk-Rock method (e.g., Słowakiewicz et al., 2015). The generated total organic carbon (TOC) and inorganic C (MINC) data were previously reported by Emmings et al. (2019).

Total carbon (C) and sulphur (TS) concentrations were measured on 110 samples using a LECO CS 230 elemental analyser. Major and trace element concentrations were measured on fused beads (109 samples) and powder briquettes (108 samples) with a PANalytical Axios

Advanced X-Ray Fluorescence (XRF) spectrometer using default PANalytical SuperQ conditions. "Excess Si" (sensu. Sholkovitz and Price, 1980) was calculated by Emmings et al. (2019) and interpreted primarily as a pelagic and biogenic (radiolarian) signal that did not migrate significantly during diagenesis. Trace element enrichment factors (EFs) (e.g., Tribovillard et al., 2006) were utilized to normalize to abundances to the detrital fraction (Eq. 1), using Post-Archaean Average Shale (PAAS) (Taylor and McLennan, 1985). X is the element concentration (major elements; wt.% and trace elements; ppm).

$$EF_{element} = \left[\frac{X}{Al}\right]_{sample} / \left[\frac{X}{Al}\right]_{PAAS} \quad (1)$$

Fe species concentration data for 99 samples were measured via sequential extraction of "highly reactive" Fe (Fe_{HR}; Poulton and Canfield, 2005; Eq. 2) phases, including carbonate-associated Fe (Fe_{carb}; e.g., siderite and ankerite), ferric (oxyhydr)oxides ($Fe_{ox;}$ e.g., goethite, haematite) and magnetite (Fe_{mag}). The extraction is a simplification of the method of Poulton and Canfield (2005). Fe_{carb}, Fe_{ox} and Fe_{mag} concentrations were measured using an Atomic Absorption Spectrometer (AAS).

The pyrite (Fe_{py}) fraction was estimated via extraction of sulphide S liberated by boiling chromous chloride solution, and titrated as Ag_2S (Canfield et al., 1986). This followed extraction of HCl-soluble (acid-volatile, Fe_{AVS}) sulphide S, in boiling HCl (Canfield et al., 1986), although in all samples Fe_{AVS} was only present as a trace component (below the limit of determination). Fe_{HR}/Fe_T (Fe_T; total Fe) and Fe_{py}/Fe_{HR} are compared with established thresholds for redox (Poulton and Canfield, 2011; Poulton and Raiswell, 2002; Raiswell and Canfield, 1998). Facies H–I Fe_{HR} is presented on a Fe_{mag}-free basis, due to the likely input of detrital Fe_{mag} (see Emmings, 2018).

$$Fe_{HR} = Fe_{carb} + Fe_{ox} + Fe_{mag} + Fe_{py} \quad (2)$$

37 sample powders (~1 g) were washed for 24 h in 200 ml 10 wt/vol % NaCl in order to leach free sulphate (Kampschulte et al., 2001). Total S measured on NaCl-washed residues was compared with the total S of untreated powders, yielding an estimate for the sulphate S (S_{sul}) fraction, after correction for the mass loss assuming leaching of pure $CaSO_4$ (Appendix B). In most cases, estimated S_{sul} was within or close to ±0.08 wt.% of the total (untreated) S (i.e., the long-term analytical precision). Therefore S_{sul} is negligible for most samples. S_{org} content was estimated by subtraction of S_{py} (Fe_{py}*1.15) and S_{sul} from TS (Eq. 3) (e.g., Tribovillard et al., 2001). Propagating the precision of TS, S_{py} and S_{sul} in quadrature yields a precision estimate of ±0.12 wt.% S_{org}.

$$S_{org} = TS - S_{py} - S_{sul} \quad (3)$$

S isotope ratios for chromium-reducible (S_{py}) extracts (as Ag_2S) were measured using a Thermo Finnigan Continuous Flow-Elemental Analysis-Isotope Ratio Mass Spectrometry (CF-EA-IRMS) system, comprising a Delta Plus XL isotope ratio mass spectrometer interfaced with a Flash 1112 elemental analyser. $^{36}S/^{34}S$ ratios of pyrite S are reported using $\delta^{34}S_{py}$ (‰) notation on the VCDT scale. S isotope ratios were drift-corrected using IAEA-S-3 (−32.3‰ VCDT) and calibrated using a linear two-point fit through IAEA-S-1 (−0.3‰ VCDT) and IAEA-S-3. $\delta^{34}S_{py}$ precision is estimated at ±1.0‰, based on two standard deviations of repeat analyses, including IAEA-S-2 (+22.7‰ VCDT). Scanning electron microscopy (SEM) was conducted on uncoated ultrathin sections using an S-3600N Hitachi microscope with Oxford INCA 350 EDS. Electron microphotographs were acquired using backscattered electrons (BSE) at 15 kV accelerating voltage, 50–66 μA filament current, in low-vacuum mode (25 Pa) and 15.0–16.3 mm (typically 16.1) working distance (WD).

4. Results and discussion

4.1. Palynofacies and paleoredox

The palynofacies assemblage in sedimentary Facies A–G (see Fig. 2) is dominated by AOM, while spores and phytoclasts are a minor component (<20%), and marine palynomorphs are absent (Fig. 2; Table 1). In Facies H–I at Cominco S9, spores and phytoclasts are dominant (Fig. 3; Table 1). Nearly all AOM is "heterogeneous" (e.g., Tyson, 1995) and subdivided into two main types; "sharp-edged, pellet-like" AOM (AOMpel; Plate I) and "granular" AOM (AOMgr; Plate II). AOMgr is rare in Facies A–F and is the dominant type of AOM in Facies G, whereas AOMpel is dominant Facies A–F and rare in Facies G.

Plotting heterogeneous AOM versus phytoclasts versus spores (Fig. 4) demonstrates most Facies A–G samples are sited in the "distal suboxic–anoxic basin" and "distal dysoxic–anoxic shelf" fields of Tyson (1995). Anoxic conditions in bottom waters during deposition of Facies A–F sediments are supported by enrichment in redox-sensitive trace elements Mo and U (e.g., Tribovillard et al., 2006) and $Fe_{HR}/Fe_T > 0.38$ (Figs. 2, 4–5; Table 1) (Poulton and Raiswell, 2002; Raiswell and Canfield, 1998). Facies H–I samples at Cominco S9 are sited in the "heterolithic oxic (proximal) shelf" and "mud-dominated oxic (distal) shelf" fields of Tyson (1995), respectively. Bottom water ventilation during deposition of Facies H–I is consistent with a lack of enrichment in Mo and U and $Fe_{HR}/Fe_T < 0.38$ (Figs. 2, 4–5; Table 1). Morridge Formation palynofacies data from the Edale Gulf and Widmerpool Gulf (Hennissen et al., 2017) plot along a mixing line between the "distal suboxic-anoxic basin" and "marginal dysoxic-anoxic basin" fields of Tyson (1995).

AOMpel is not comparable to AOM in contemporaneous mudstones from the nearby Widmerpool Gulf paralic basin (Fig. 1a) (Hennissen et al., 2017; Könitzer et al., 2016), but is similar to a variety of "well-preserved" AOM with Type I and II composition. "Well-preserved" AOM is observed in the Kimmeridge Clay (Tyson, 1989; Tyson, 1995) and relatively aliphatic (H-rich) intervals from the Bowland Shale in the Edale Gulf (Fig. 1a) (Hennissen et al., 2017), for example. AOMpel typically exhibits pellet-like geometries (e.g., Plate I, 3, 5, 7). Thus AOMpel most likely represent the fecal minipellets of zooplankton (e.g., Stoecker, 1984; Gowing and Silver, 1985; Beaumont et al., 2002; Lampitt et al., 2009) and/or fecal pellets of macro-zooplankton (e.g., Porter and Robbins, 1981; Bruland and Silver, 1981; Cuomo and Chen, 1996; Henschke et al., 2016).

AOMgr (Plate II) exhibits a large particle diameter (500 μm, i.e., limit of the mesh size), sheet-like, fragmented character (Plate II, 4) and contains candidate organic sheaths (Plate II, 6, 7). AOMgr is comparable to "diffuse-edged AOM" (Tyson, 1995) and most AOM in contemporaneous mudstones from the paralic Widmerpool Gulf (Fig. 1a), including AOMgr described by Hennissen et al. (2017), and AOMGr and possibly AOMBr described by Könitzer et al. (2016). The relative abundance of AOMgr increases significantly above the transition from anoxic (Facies F) to suboxic or oxic (Facies G) bottom waters, indicated by a loss of enrichment of redox sensitive trace elements, such as Mo and U (e.g., Tribovillard et al., 2006), Fe_{HR}/Fe_T close to 0.38 (Poulton and Raiswell, 2002; Raiswell and Canfield, 1998), and bioturbation in Facies G (Emmings et al., 2019). AOMgr dominates the palynofacies assemblage in Facies G (Fig. 2; Table 1) so that Facies G is sited in the "distal suboxic–anoxic basin" and "distal dysoxic–anoxic shelf" fields of Tyson (1995) (Figs. 4–5). This is slightly inconsistent with the paleoredox proxy record which suggests deposition under dominantly oxic or suboxic conditions.

Presence of pyritized burrows, and early diagenetic nodular, aggregated and large framboidal pyrite forms in Facies G (Emmings et al., 2019) suggests highly sulphidic, and advective or stagnant conditions existed near seabed (Rickard, 2012). This is supported by high $\delta^{34}S_{py}$ values in Facies G (Fig. 2; Table 1; +6.4 and −8.9‰), which shows the bulk pyrite population formed under closed system conditions

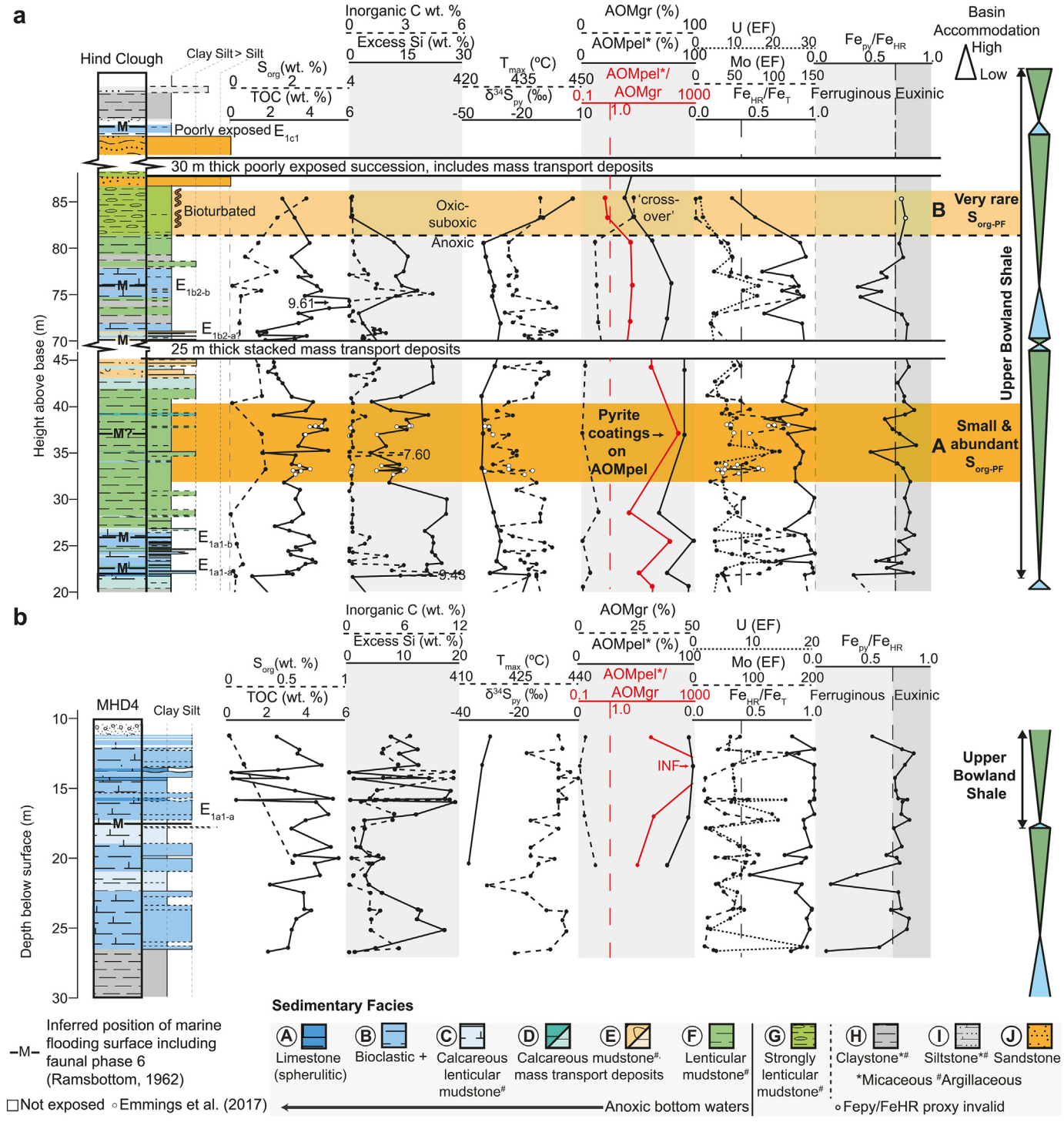

Fig. 2. Sedimentary logs through Hind Clough (a) and borehole MHD4 (b), from Emmings et al. (2019), plotted with selected geochemical data including RockEval pyrolysis total organic carbon (TOC), inorganic C content and T_{max}, organic S (S_{org}), bulk pyrite $\delta^{34}S_{py}$, enrichment factors (EFs) for redox-sensitive trace elements (Mo, U) and Fe speciation redox proxies. See Materials and Methods for derivation of "excess Si" and calculation of trace element enrichment factors (EFs). Intervals A and B exhibit relatively high S_{org} content. Interval A contains abundant sulphurized AOM spheres surrounding pyrite framboids ($S_{org\text{-}PF}$).

(e.g., Nissenbaum et al., 1972; Mossmann et al., 1991; Canfield et al., 1992). On this basis, AOMgr likely represents the remnants of extracellular polysaccharides (e.g., Pacton et al., 2007, 2011) produced by benthic microbial mats. This is supported by sedimentological interpretations (Emmings et al., 2019). Such mats potentially colonized a niche environment at the seabed as chemoautotrophic or chemoheterotrophic sulphide-oxidizers (e.g., Grunke et al., 2011).

4.2. Mechanisms for sulphurization

Intervals "A" (within Facies F) and "B" (Facies G) exhibit $S_{org}/TOC > 0.04$, suggesting a bulk Type II-S kerogen composition (Orr, 1986). A microbial mat origin to AOMgr may explain the exceptionally high S_{org} content in Interval B (Facies G). Modern microbial mats oxidize H_2S using O_2 or NO_3^- as an electron acceptor across a strong redox gradient

Table 1
Selected palynofacies abundances and geochemical data.

Sample	Depth / Height (m)	Location	Facies	AOMpel* (%)	AOMgr (%)	TOM (%)	Total AOM (%)	AOMpel/ AOMgr	TOM/ AOMpel	T_{max} (°C)	TOC (%)	MINC (%)	S (%)	S_{py} (%)	S_{sul} (%)	S_{org} (%)	Atomic S/C	$\delta^{34}S_{py}$ (‰)	Fe_{HR}/ Fe_T	Fe_{py}/ Fe_{HR}	Mo (EF)	U (EF)
SSK61352	11.9	C-S9	I	10.1	11.0	78.8	21.1	0.9	7.8	457	2.17	0.30	0.047	0.04	0.01	<LLD	-	–8.6	0.25	0.04	1.00	0.80
SSK61392	33.28	C-S9	H	11.4	7.2	83.3	18.6	1.6	7.3	456	3.26	0.28	0.14	0.09	-	<LLD	-	–	0.3	0.08	1.10	0.8
SSK61404	40.72	C-S9	B	53.0	15.2	31.9	68.2	3.5	0.6	445	3.42	1.63	1.61	1.47	0.10	0.04	0.00	–32.1	0.72	0.67	26.60	5.80
SSK61420	49.74	C-S9	F	42.6	10.4	46.8	53.0	4.1	1.1	443	1.95	0.12	3.07	2.95	0.28	<LLD	-	–24.4	0.64	0.83	2.70	1.4
HC02_198	114	HC	F	49.5	11.1	39.4	60.6	4.5	0.8	433	3.1	0.2	0.22	0.09	0.05	0.08	0.01	–35.5	-	-	6.7	3.1
HC02_191	85.7	HC	G	36.9	45.6	17.6	82.5	0.8	0.5	440	2.7	0.2	4.05	1.23	0.26	2.56	0.34	6.4	0.31	0.74	2.9	2.0
HC02_188	83.6	HC	G	44.5	45.9	9.3	90.4	1.0	0.2	440	3.3	0.2	3.61	1.93	0.12	1.56	0.17	–8.9	0.51	0.78	3.3	2.7
HC02_184	80.83	HC	F	62.4	11.7	26.0	74.1	5.3	0.4	432	4.1	0.2	4.81	3.66	0.24	0.91	0.08	–39.5	0.90	0.73	48.9	7.0
HC02_174	76.1	HC	B	76.9	13.0	10.1	89.9	5.9	0.1	432	4.5	1.5	3.51	2.04	1.37	0.10	0.01	–34.0	0.88	0.37	143.9	15.9
HC02_166	72.02	HC	F	72.5	14.4	13.0	86.9	5.0	0.2	433	3.5	0.2	3.63	3.27	0.08	0.27	0.03	–30.8	0.91	0.79	25.1	4.5
HC02_127	62.78	HC	B	54.9	26.1	19.1	81.0	2.1	0.3	433	4.92	0.21	2.90	2.56	<LLD	0.34	0.02	–37.2	1.00	0.73	137.8	7.9
HC02_125	62.44	HC	D	87.4	8.8	3.8	96.2	9.9	0.0	437	1.59	3.19	1.43	1.19	0.13	0.11	0.02	–27.9	1.00	0.55	108.6	15.7
HC02_120	61.6	HC	Em	89.5	3.0	7.6	92.5	29.8	0.1	437	1.61	0.08	0.45	0.51	<LLD	<LLD	-	–27.0	0.75	0.75	18.1	5.3
HC02_106	56.35	HC	E	65.4	20.5	14.2	85.9	3.2	0.2	439	3.45	1.71	2.81	2.07	0.12	0.63	0.06	–29.7	0.75	0.60	26.4	6.2
HC02_101	54.7	HC	E	93.9	1.5	4.8	95.4	62.6	0.1	439	2.43	0.38	1.61	1.48	0.05	0.08	0.01	–24.8	0.92	0.70	21.5	4.8
HC02_87	51.86	HC	E	77.2	11.9	10.9	89.1	6.5	0.1	435	3.77	1.21	3.72	2.71	0.52	0.50	0.05	–34.3	0.80	0.73	50.8	8.6
HC02_75	48.82	HC	E	63.1	23.0	13.9	86.1	2.7	0.2	442	1.71	1.13	1.75	1.23	0.09	0.44	0.09	–23.0	0.73	0.63	19.8	4.2
HC02_73	48.14	HC	Em	87.9	3.2	8.8	91.1	27.5	0.1	440	2.19	1.14	2.40	1.75	0.16	0.49	0.08	–28.5	0.82	0.65	34.4	5.5
HC02_67	44.77	HC	E	87.9	3.0	9.2	90.9	29.3	0.1	431	2.27	1.57	3.94	2.88	0.12	0.93	0.15	–34.1	0.81	0.73	64.6	9.7
HC01_04B#	37.37	HC	F	84.8	0.4	14.5	85.2	212.0	0.2	432	3.87	0.09	4.88	2.94	0.89	1.05	0.10	–40.1	0.77	0.65	77.5	9.7
HC02_37	28.7	HC	F	68.4	14.6	17.0	83.0	4.7	0.2	440	3.75	0.17	1.16	0.97	0.20	<LLD	-	–34.6	0.95	0.74	47.6	10.4
HC02_31	25.52	HC	C	97.8	0.7	1.4	98.5	139.7	0.0	441	4.33	0.82	1.25	0.97	0.09	0.19	0.02	–31.0	0.94	0.65	72.5	5.1
HC02_21	22.02	HC	B	73.1	7.4	19.6	80.5	9.9	0.3	441	2.92	0	2.28	2.12	<LLD	0.16	0.02	–36.5	0.99	0.77	91.7	6.8
HC02_16	16.4	HC	B	91.4	3.2	5.2	94.6	28.6	0.1	442	3.55	3.65	1.29	1.16	0.07	0.06	0.01	–25.3	0.98	0.65	66.9	3.5
HC02_14	12.9	HC	B	49.6	15.5	35.0	65.1	3.2	0.7	441	2.95	3.66	1.75	1.56	0.06	0.13	0.02	–33.0	0.86	0.61	55.4	3.5
HC02_13	11.6	HC	B	72.7	12.8	14.5	85.5	5.7	0.2	442	3.31	2.03	1.73	1.48	0.16	0.13	0.01	–30.1	1.00	0.76	49.6	4.8
HC02_11	5.9	HC	D	76.3	5.2	18.3	81.5	14.7	0.2	436	2.18	4.04	3.01	2.61	0.21	0.19	0.03	–29.6	0.91	0.73	36.9	10.8
HC02_2	0.68	HC	B	77.1	10.3	12.5	87.4	7.5	0.2	442	3.43	3.09	2.09	1.75	0.13	0.21	0.02	–30.8	0.96	0.77	43.0	4.4
SSK60768	10.8	MHD4	A	95.3	2.6	2.1	97.9	36.7	0.0	435	2.66	6.78	1.04	0.91	0.12	0.01	0.00	–29.3	0.82	0.51	74.8	5.8
SSK60774	12.9	MHD4	B	99.8	0	0.1	99.8	INF	0.0	435	4.87	5.51	2.15	1.87	0.14	0.14	0.01	–32.1	1.00	0.80	64.2	6.2
SSK60787	16.55	MHD4	B	95.4	2.1	2.3	97.5	45.4	0.0	435	5.2	5.09	1.81	1.55	0.51	<LLD	-	–34.6	1.00	0.77	49.6	12.9
SSK60798	20.18	MHD4	B	75.2	7.0	17.9	82.2	10.7	0.2	430	4.54	2.41	4.92	3.72	0.65	0.55	0.04	–36.7	0.89	0.75	98.6	8.4

*This fraction is dominated by AOMpel (including AOMpyr) but also includes other possible sub-types of heterogeneous, sharp-edged AOM. See Emmings et al. (2019) for sedimentary facies description and interpretations. See Emmings (2018) for Fe-speciation and Mo and U data and interpretations. Facies E and Em likely represent mass transport deposits (Emmings et al., 2019), and therefore contain Sorg-rich AOMgr as rip-up clasts. Highlighted rows indicate Interval A (bottom) and B (top) as detailed in Fig. 2. TOM = terrestrial palynomorphs (spores) and phytoclasts. MINC = inorganic C. C-S9 = Cominco S9. HC = Hind Clough. MHD4 = Marl Hill 4. Facies H-I Fe_{HR} is presented on a Fe_{mag}-free basis, due to the likely input of detrital Fe_{mag} (see Emmings, 2018 for discussion). #RockEval pyrolysis and major and trace element data reported by Emmings et al. (2017).

at the seabed (Bailey et al., 2009; Canfield and Teske, 1996; Grunke et al., 2011; Sievert et al., 2007; Wirsen et al., 2002), and are consortia of several different types of bacteria. AOMgr is probably most comparable to the colorless sulphur bacterium *Arcobacter* (phylum Proteobacteria) that produces a "cotton-ball"-like structure (Grunke et al., 2011; Wirsen et al., 2002) via fixation of S_{org} in filaments

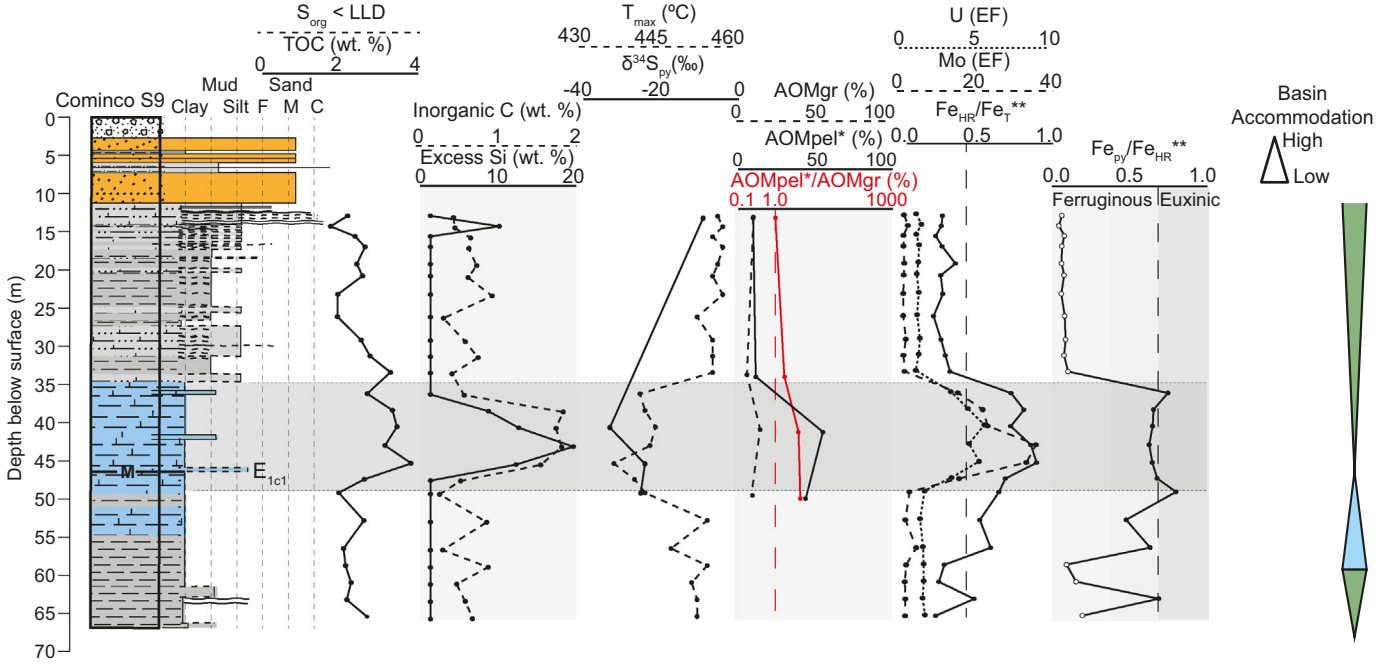

Fig. 3. Sedimentary log through borehole Cominco S9, from Emmings et al. (2019), plotted with selected geochemical data including RockEval pyrolysis total organic carbon (TOC), inorganic C content and T_{max}, organic S (S_{org}), bulk pyrite $\delta^{34}S_{py}$, enrichment factors (EFs) for redox-sensitive trace elements (Mo, U) and Fe speciation redox proxies. See Materials and Methods for derivation of "excess Si" and calculation of trace element enrichment factors (EFs). See Fig. 2 for key to sedimentary facies. **Facies H-I Fe_{HR} is presented on a Fe_{mag}-free basis, due to the likely input of detrital Fe_{mag} (see Emmings, 2018 for discussion).

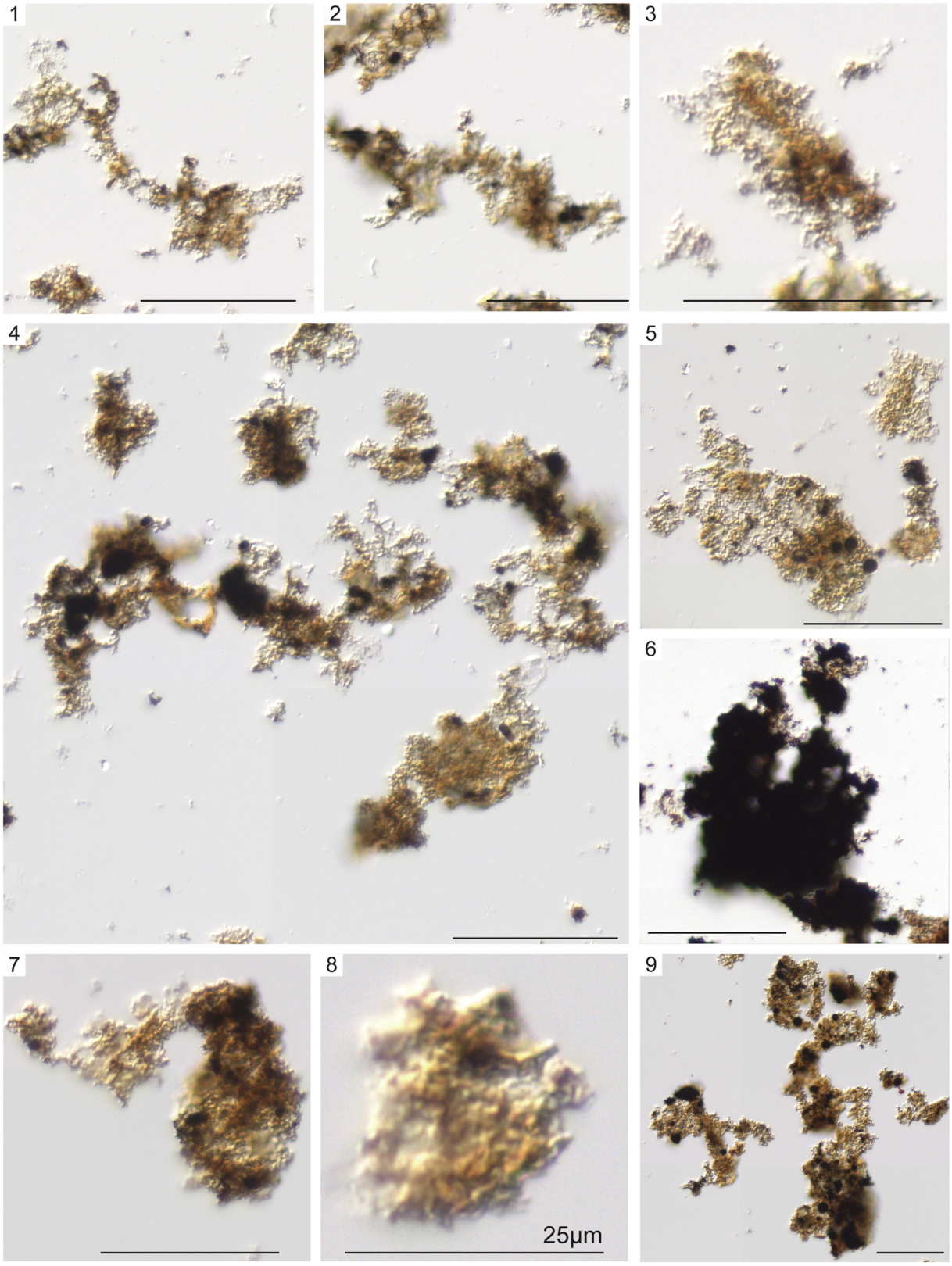

Plate I. "Sharp-edged" heterogeneous amorphous organic matter (AOMpel) example transmitted light microphotographs. Scale bars = 50 μm unless otherwise stated. 1–4. MPA68143. 5. MPA68144. 6. MPA66949. 7–9. MPA68145.

(Steudel, 1989). *Arcobacter* mats are present at cold seeps on the Nile Deep Sea Fan (Grunke et al., 2011), for example. AOMgr may also be comparable to *Thiopoloca*, a sulphide-oxidizing denitrifier that is widespread beneath the upwelling Peru-Chile upwelling region (Fossing et al., 1995). Alternatively, the high S_{org} content in Interval A may be explained by direct reaction of H_2S with OM (e.g., Sinninghe Damsté and De Leeuw, 1990a; Amrani, 2014). Regardless of S fixation mechanism, stagnation or advection of sulphidic porwaters near seabed implies

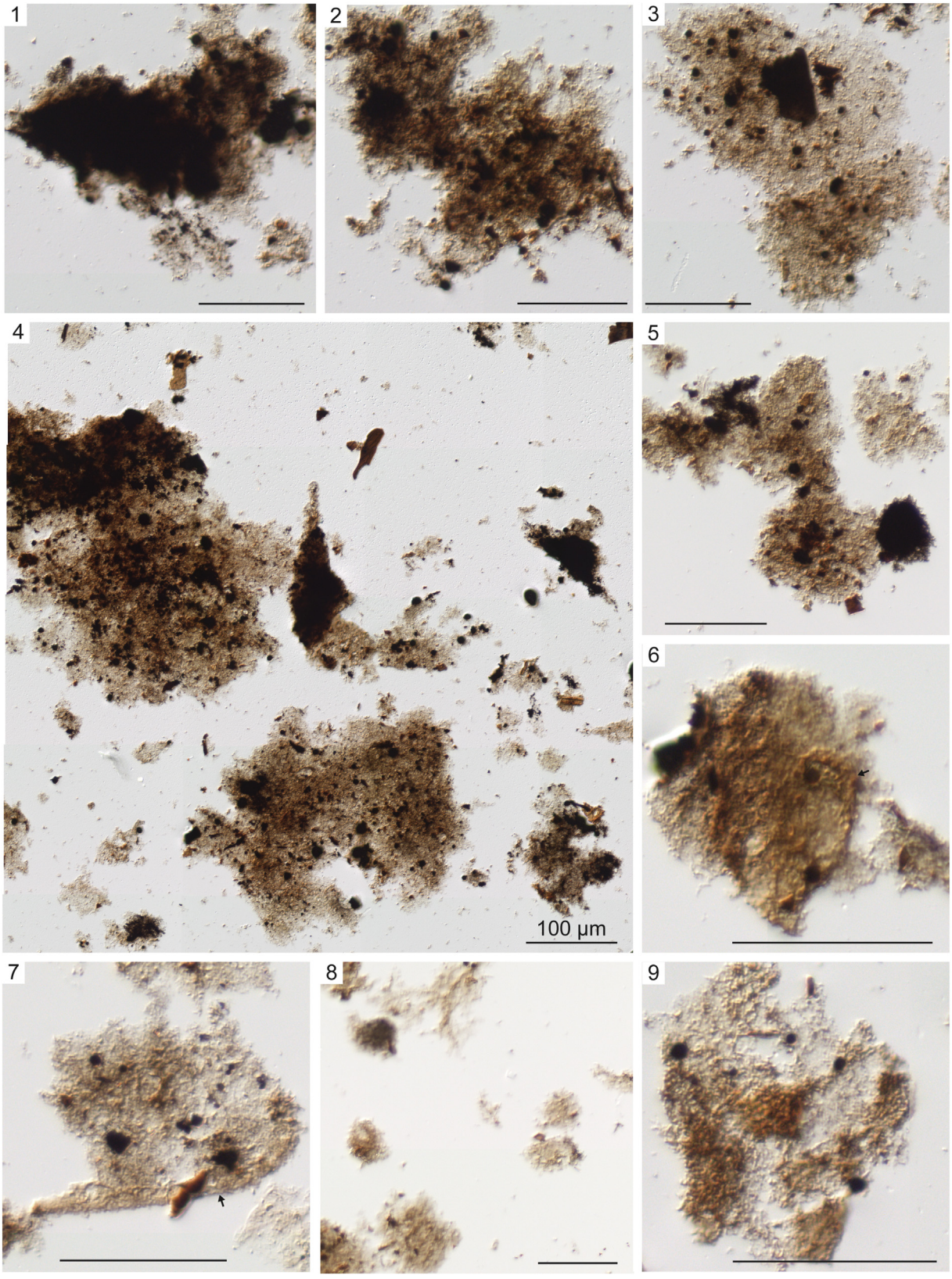

Plate II. "Diffuse-edged, granular" heterogeneous amorphous organic matter (AOMgr) example transmitted light microphotographs. Scale bars = 50 µm unless otherwise stated. 1–4. MPA68138. 5–7. MPA68139 (6–7, arrows indicate candidate sheaths). 8. MPA68140. 9. MPA68128.

relatively vigorous and sustained rates of SO_4-reduction (as the likely source of sulphide) and/or minimal buffering by reactive Fe in underlying sediments.

Ancient examples of benthic microbial mats are rare (Catuneanu, 2007; Schieber, 1986; Schieber et al., 2007a; Schieber et al., 2007b; Seckbach and Oren, 2010), especially regarding chemotrophs (Bailey

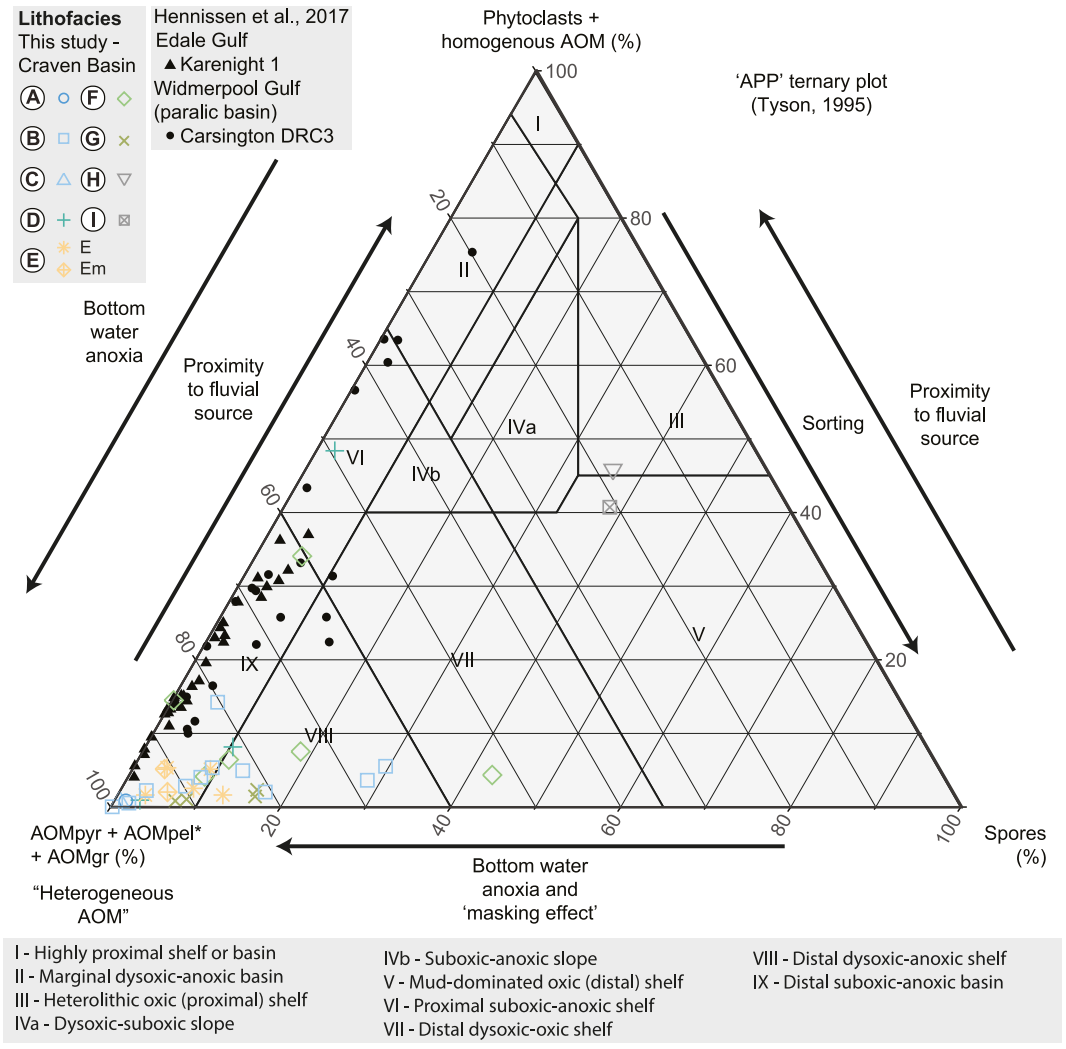

Fig. 4. "APP" ternary plot of heregeneous AOM (defined as AOMpyr + AOMpel + AOMgr) versus phytoclasts + homogenous AOM (the latter is typically negligible in samples in this study) versus spores (terrestrial palynomorphs). Fields and interpreted processes are from Tyson (1995). Reprinted/adapted by permission from Springer Nature Customer Service Centre GmbH: Springer Nature, Sedimentary Organic Matter: Organic Facies and Palynofacies by Tyson, R. V. © 1995. See Fig. 2 and Emmings et al. (2019) for sedimentary facies description. Palynofacies abundance data for the Morridge Formation in the Edale Gulf (borehole Karenight 1) and Widmerpool Gulf (borehole Carsington DRC3), from Hennissen et al. (2017), are also plotted for comparison.

et al., 2009). Early silica-cemented chemotrophic microbial mats are present in the Miocene Monterey Formation (Williams, 1984), which potentially contributed significantly to the petroleum system and Type II-S kerogen composition (Orr, 1986; Williams, 1984). S-rich filaments in modern chemosynthetic microbial mats can be sheathed by OM (Wirsen et al., 2002). Such sheaths are possibly observed within AOMgr (Plate II, 6, 7), although these are not a universal feature (Wirsen et al., 2002), and are not always preserved (Grant, 1991). Sulphide is toxic to infauna (Wang and Chapman, 1999). Thus predators to mats, such as gastropods (e.g., Tribovillard et al., 2000), were likely occluded from this environment due to the high redox gradient at seabed.

Interval A in Facies F overlying the E_{1a1} marine band exhibits relatively high S_{org} content yet contains minimal AOMgr (Fig. 2; Table 1). This package is distinctive because the palynological fraction is dominated by AOMpel that is coated by fine, microcrystalline pyrite ("AOMpyr"; Plate I, 6). AOMpel in Interval A also contains abundant orange, high-relief organic spheres within each particle (Plate III). Rarely, these spheres are also present within AOMgr in Facies G (Interval B; Fig. 2; Plate III, 6–9).

The spheres exhibit a finely reticulated texture in transmitted light that mimics pyrite framboids (Plate III, 3), and are best observed in oxidized slides following removal of the microcrystalline pyrite coatings on AOM. In some cases, each sphere contains a single pyrite framboid (Plate III, 1). The diameter of organic spheres in Interval A (Fig. 6) is similar to pyrite framboids in Facies F (Emmings et al., 2019). The orange color of the organic spheres suggests sulphurized OM (e.g., Tribovillard et al., 2001), possibly comparable to orange gel-like AOM "drops" (Aycard et al., 2003). AOM sulphurization is consistent with the relatively high S_{org} content in Interval A. The catalytic effect of S radicals associated with S_{org} during the thermal decomposition of kerogen (Lewan, 1998) may also explain the relatively low Rock-Eval T_{max} through Interval A. T_{max} through Interval A is approximately 15 °C lower than the adjacent mudstone packages (Figs. 2, 7; Table 1). Such T_{max} inversions are not necessarily diagnostic of Type II-S OM, however, because a similar reduction in T_{max} is observed through the E_{1c1} marine band at Cominco S9 despite very low S_{org} content (Fig. 3). This suggests T_{max} is also influenced more broadly by OM composition (Type II versus III) and/or mineral matrix effects.

Sphere fluorescence under green light (Plate III, 5, 7, 9) suggests the presence of aromatic compounds within a moderately polymerized structure (Lin and Davis, 1988), potentially including S heteroatoms such as thiophenes (e.g., Eglinton et al., 1990). Since AOMgr in Interval B lacks fluorescence under green light and generally lacks $S_{org\text{-}PF}$, this

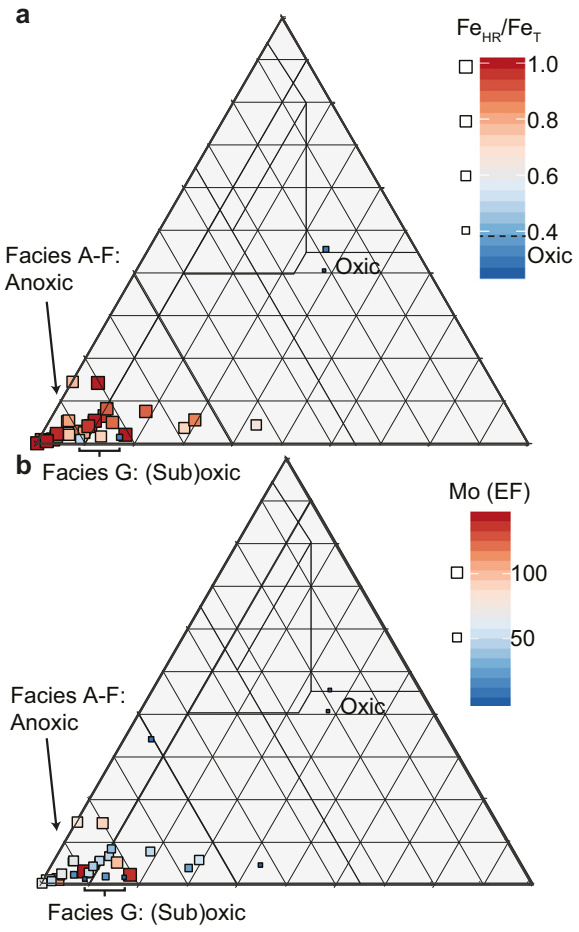

Fig. 5. "APP" ternary plot (see Fig. 4 for details) with paleoredox proxies (a) Fe_{HR}/Fe_T and (b) Mo enrichment factors (EFs) mapped to each sample. See text for discussion.

suggests most S_{org} is present as (non-fluorescing) cross-linked (intermolecular) S polymers (e.g., Aizenshtat et al., 1995; Sinninghe Damsté et al., 1989).

The orange spherical texture in AOM is termed "$S_{org\text{-}PF}$," and is comparable to the texture originally described by Love (1957, 1962). Pyrite framboids are present in all sedimentary facies (Emmings et al., 2019), yet $S_{org\text{-}PF}$ is only present in interval A, and rarely interval B. Clearly the microenvironment surrounding pyrite framboids within OM promoted sulphurization. Sulphurization of OM requires access to compounds prone to complexation with S (Adam et al., 2000) and available reactive S species in the local microenvironment. O contained within carbonyl groups, in particular, is prone to replacement by reduced S (e.g., Adam et al., 2000). Carbohydrates are also susceptible to sulphurization (Van Kaam-Peters et al., 1998). Reactive S species include H_2S, polysulphides, sulphites, or other S of intermediate oxidation states (Aizenshtat et al., 1995; Amrani, 2014; Amrani and Aizenshtat, 2004; Rickard, 2012; Sinninghe Damsté and Leeuw, 1990b; Wasmund et al., 2017).

Under anoxic conditions, "redox oscillation" between zones of SO_4 and Fe reduction (sensu. Aller, 1982; Aller, 1998) promotes sulphurization (Aplin and Macquaker, 1993; Filley et al., 2002) via S cycling and therefore generation of reactive S species (e.g., Wasmund et al., 2017). Redox oscillation also enhances oxidation and/or dehydration of low-molecular weight compounds, such as alcohols, producing aldehydes or ketones (i.e., compounds with carbonyl functional groups; Burdige, 2006). These compounds are thought to be particularly susceptible to sulphurization, especially if they contain conjugate double bonds (Adam et al., 2000; Aizenshtat et al., 1995; Amrani, 2014; Grossi et al., 1998; Rontani et al., 1999).

Therefore redox oscillation *localized* to OM is the best explanation for $S_{org\text{-}PF}$ formation. This differs from the mechanism of sulphurization under persistently sulphidic (euxinic) conditions (e.g., Lewan, 1984; Orr, 1986; Hartgers et al., 1997), where H_2S potentially reacts directly with OM (Amrani, 2014; Sinninghe Damsté and De Leeuw, 1990a). Under oscillatory redox conditions during early diagenesis, H_2S generation via SO_4-reduction likely proceeded only within the microenvironment local to particles of metabolizable OM (e.g., Burdige, 2006). This is consistent with the presence of pyrite that apparently nucleated on and/or within AOMpel within Interval A (Plate I, 6).

Early diagenetic redox oscillation within Interval A is consistent with the Mo and U and $\delta^{34}S_{py}$ record (Table 1; Fig. 2). Firstly, high Mo relative to U in Interval A (Facies F mean Mo EF ~ 76 ± 86, U EF ~ 8 ± 3) suggests the presence of a relatively weak and unstable water column chemocline and development of "particulate shuttle" conditions (Algeo and Tribovillard, 2009). This contrasts with moderate to high Mo *and* U contents in "marine band" Facies A–C (mean Mo EF ~ 32 ± 39, U EF ~ 11 ± 11), which suggests relatively stable, moderately sulphidic conditions in bottom waters. Secondly, strongly negative (close to −40‰) $\delta^{34}S_{py}$ in Interval A suggests pyrite precipitation under long-lived open-system conditions and/or large S fractionations via intermediate S cycling (e.g., Nissenbaum et al., 1972; Mossmann et al., 1991; Canfield et al., 1992; Canfield et al., 2010).

H_2S that migrated into surrounding porewaters was likely oxidized to produce sulphuric acid (e.g., Soetaert et al., 2007). This explains the lack of carbonate (Fig. 2), despite the presence of skeletal moulds (Emmings et al., 2019), in Intervals A and B. Therefore the contacts between OM microenvironments and adjacent porewaters exhibited an intermittently high redox-gradient (Fig. 8). This gradient was likely strongest during periods of redoxcline deepening, where porewaters were flooded by Fe-reducers. S cycling across these micro-redox fronts, local to each framboid, provided the reactive S species required for sulphurization.

Pyrite nucleation within AOM likely formed initially as FeS, via reaction with dissolved reduced Fe, sourced via dissimilatory Fe^{3+} reduction or direct reduction of particulate FeOOH by H_2S (Fig. 8). FeS subsequently reacted with H_2S and/or polysulphides to produce pyrite (e.g., Rickard, 2012). Microcrystalline pyrite coatings on OM (Plate I, 6) are therefore interpreted as a relict redox front, defined by reaction of H_2S generated local to OM, and Fe^{3+} and/or FeOOH present in the surrounding porewaters.

H_2 or short polysulphides are products of pyrite precipitation where FeS is the reactant (Soetaert et al., 2007). H_2, as a key nutrient, potentially stimulated microbial activity (Nissenbaum et al., 1972; Rickard, 2012), which in turn promoted sulphurization local to the pyrite framboids. Thus $S_{org\text{-}PF}$ formed concomitantly with, or following, pyrite (e.g., Filley et al., 2002), and are perhaps analogous to "sulphurized biofilms" (MacLean et al., 2008). Microbial oxidization of H_2 (as a nutrient) coupled to dissimilatory elemental S reduction (Aizenshtat et al., 1995; Sinninghe Damsté and De Leeuw, 1990a) also generates reactive S species (e.g., via elemental S or polysulphide-reducing bacteria; Ma et al., 1993; Ma et al., 2000; Wasmund et al., 2017).

$S_{org\text{-}PF}$ is abundant in Interval A but rare in Interval B (compare Plate III, 2 and 8), perhaps because pyrite framboids are also rare in Interval B (Emmings et al., 2019). This suggests that H_2S and/or polysulphide in porewaters seldom attained the critical supersaturation conditions required for framboid nucleation (Ohfuji and Rickard, 2005; Rickard, 2012). Together, this suggests that the steepest redox gradient during deposition of Interval B was located near or at (and parallel to) the seabed, likely utilized by microbial mats, and not local to OM. Thus pyrite nucleation and growth in Interval B was uncoupled to sites of *in situ* H_2S production driven by OM degradation, but instead driven by reaction of reduced Fe with upward-diffusing H_2S. It is also possible AOMgr, as the dominant type of particulate OM in Interval B, was relatively refractory and therefore relatively resistant to hydrolysis and degradation by microbes. This limited the production of H_2S local to OM required for framboid (and therefore $S_{org\text{-}PF}$) growth.

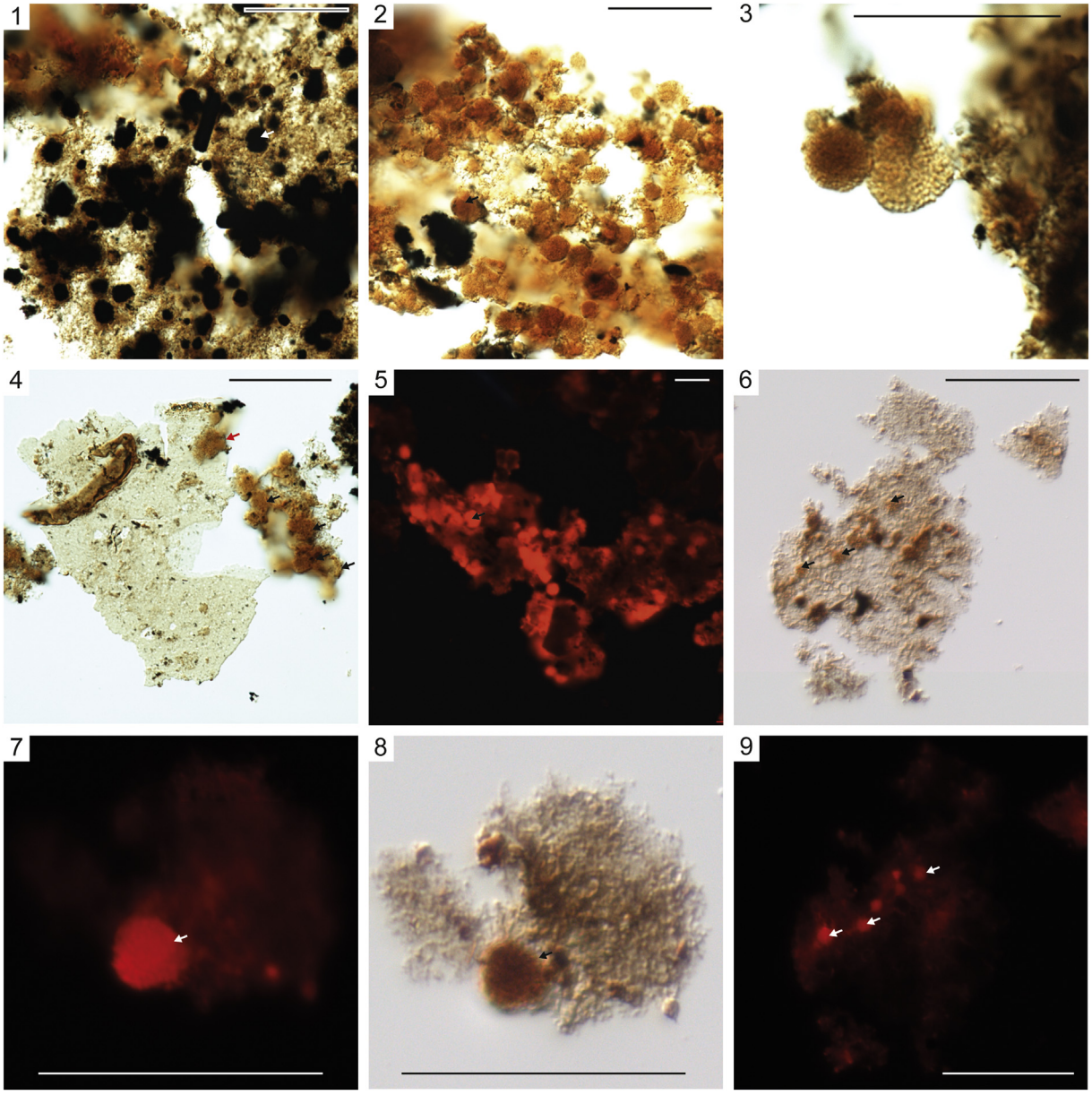

Plate III. Sulphurized AOM local to pyrite framboids ($S_{org\text{-}PF}$; arrows indicate examples). Scale bars = 50 μm. 1–5. Interval A. 1–4. MPA66949 (oxidized slide 4, transmitted light). 5. MPA66949 (oxidized slide 4, incident green light, red light filtered). 6–9. Interval B. 6, 8. MPA68139 (oxidized slide 4, transmitted light). 7, 9. (Incident green light, red light filtered).

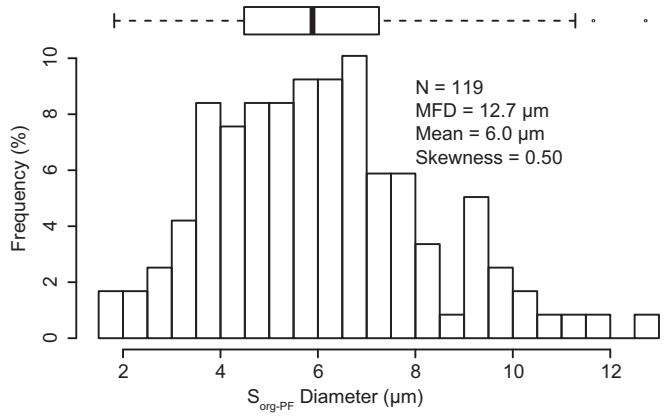

Fig. 6. $S_{org\text{-}PF}$ diameter versus frequency in Interval A (Facies F). N = number of spheres counted, MFD = maximum framboid diameter (Wignall and Newton, 1998).

4.3. Controls on organic matter distribution

The distribution of key palynofacies categories through the Upper Bowland Shale in the Craven Basin is predictable and linked to changing bottom water redox conditions and changing basin accommodation. Facies A–C muds deposited during marine transgressions (Figs. 2–4, Table 1) lack $S_{org\text{-}PF}$ likely because the redoxcline bounding zones of SO_4 and Fe reduction was fixed in the water column during deposition (Fig. 9a). Marine maximum flooding is associated with a high AOMpel/AOMgr and low abundance of spores and phytoclasts.

Intervals A and B overlie "marine band" packages and were therefore likely deposited during sea level fall (Emmings et al., 2019). An enhanced shelf-to-basin "Fe shuttle" during falling sea level (Lyons and Severmann, 2006) increased the Fe_{HR} supply to the basin (Emmings, 2018). This process promoted buffering of H_2S by Fe_{HR} via pyrite formation (including nucleation on AOM to generate AOMpyr), weakening and destabilizing the chemocline, stimulating early diagenetic redox

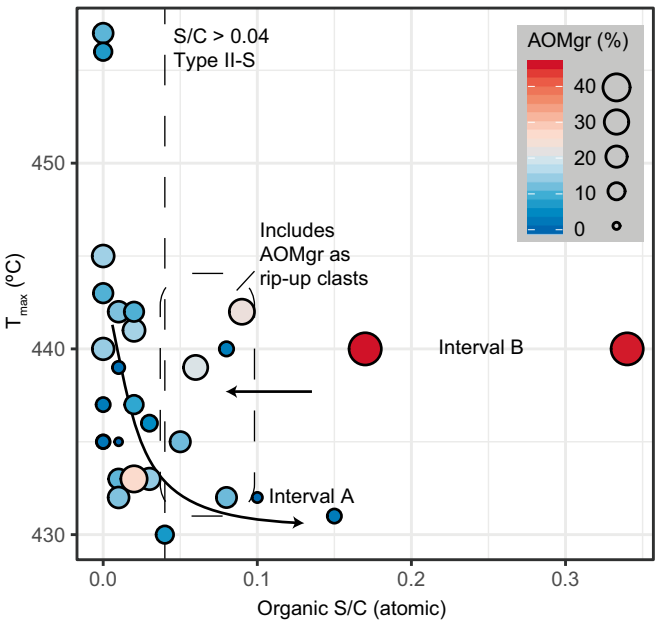

Fig. 7. Rock-Eval pyrolysis T_{max} versus organic S/C, with point size and color mapped to the relative abundance of AOMgr, and with Type II-S field (S/C > 0.04) from Orr (1986). Several turbidites, debrites and hybrid flow deposits exhibit moderate S/C and contain AOMgr interpreted as rip-up clasts (Emmings et al., 2019). Interval A is possibly positioned at the end of a mixing line defined by the catalytical effect of S radicals during hydrocarbon maturation (Lewan, 1998).

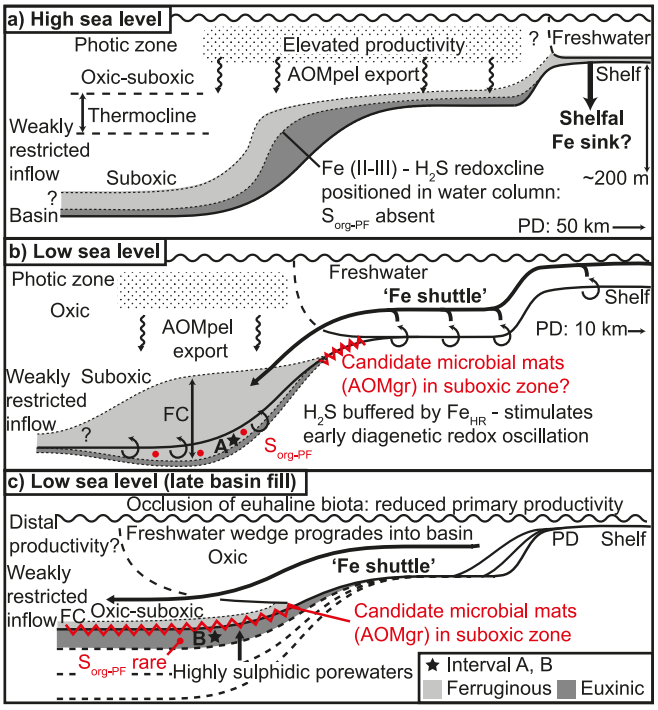

Fig. 9. Basin accommodation control on the distribution of $S_{org\text{-}PF}$, after the model for anoxia in the Craven Basin described by Emmings (2018). (a) Deposition of "marine band" facies during periods of high sea level and euxinic bottom waters driven by relatively high rates of primary productivity (enhanced AOMpel export). Fixation of the redoxcline within the water column, bounding zones of Fe and SO_4-reduction, limited $S_{org\text{-}PF}$ formation in sediments. (b) Falling sea level promoted Fe_{HR} shuttling into deep waters (via mobilization of the shelfal Fe_{HR} sink) and triggered early diagenetic redox oscillation in porewaters (likely between zones of Fe- and SO_4-reduction). These conditions promoted pyrite precipitation on AOM (AOMpyr) and $S_{org\text{-}PF}$ formation in Interval A. (c) Bottom waters became progressively oxygenated during the late stages of deposition of the Bowland Shale. AOMpel is replaced by AOMgr as the dominant type of AOM, which may represent sulphide-oxidizing microbial mats that utilized the high redox gradient near seabed. These conditions are linked to limited $S_{org\text{-}PF}$ formation but possibly promoted intermolecular fixation of S_{org} (Interval B).

oscillation and triggering $S_{org\text{-}PF}$ formation (Interval A; Fig. 9b). Therefore $S_{org\text{-}PF}$ is a proxy for redox oscillation between sulphidic and ferruginous anoxic micro-environments during early diagenesis.

Pendle delta progradation during the E_{1b2} biozone triggered euphotic zone desalination, which sufficiently reduced the export of autochthonous (marine) OM to seabed and therefore promoted bottom water oxygenation (Emmings, 2018). Bottom water ventilation promoted colonization of the seabed by sulphide-oxidizing microbial mats (Fig. 9c). Therefore the transition from anoxic (Facies F) to oxic/suboxic conditions (Facies G) exhibits a "cross-over" between AOMpel and AOMgr (Fig. 2; Table 1). The proportionality of AOMpel and AOMgr may therefore delineate ancient redox fronts at or near seabed. Palynological assessment of AOM types should be coupled with detailed sedimentological characterization, however, in order to determine whether AOMgr particles are present in situ or as rip-up clasts.

Fig. 10 integrates and summarizes observations and interpretations spanning palynology and geochemistry (this study), sedimentology

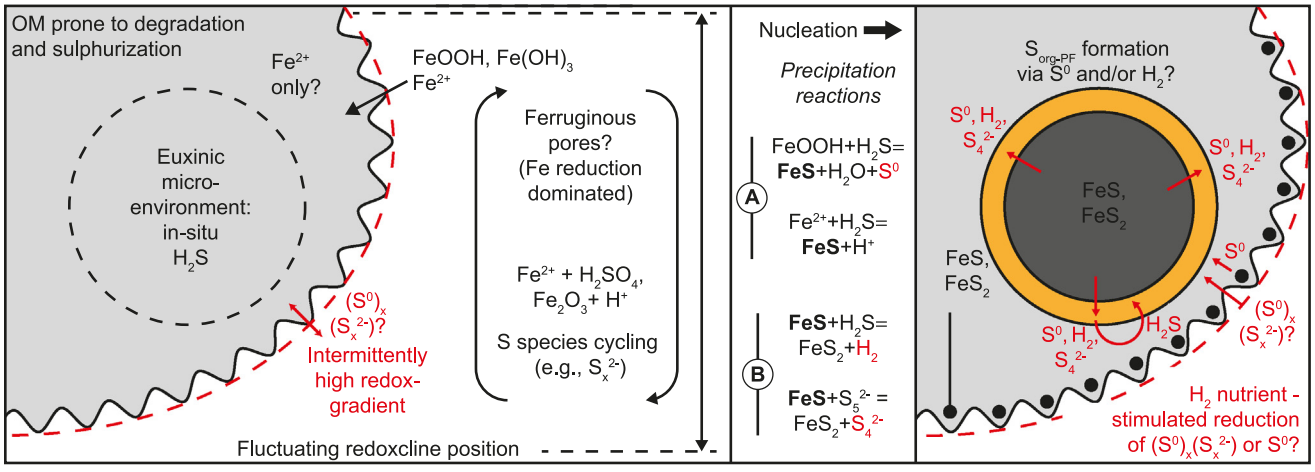

Fig. 8. Proposed mechanism for formation of $S_{org\text{-}PF}$ local to pyrite framboids in Interval A (and rarely B), via capture of reactive S species across a local redoxcline between zones of Fe- and SO_4-reduction, and/or via microbial reduction of intermediate S species perhaps via H_2 nutrient loading local to framboids. These conditions are likely favored during early diagenetic redox oscillation under relatively high Fe_{HR} loadings. Fe mono-sulphide and pyrite nucleation equations (labeled A and B, respectively) from Soetaert et al. (2007).

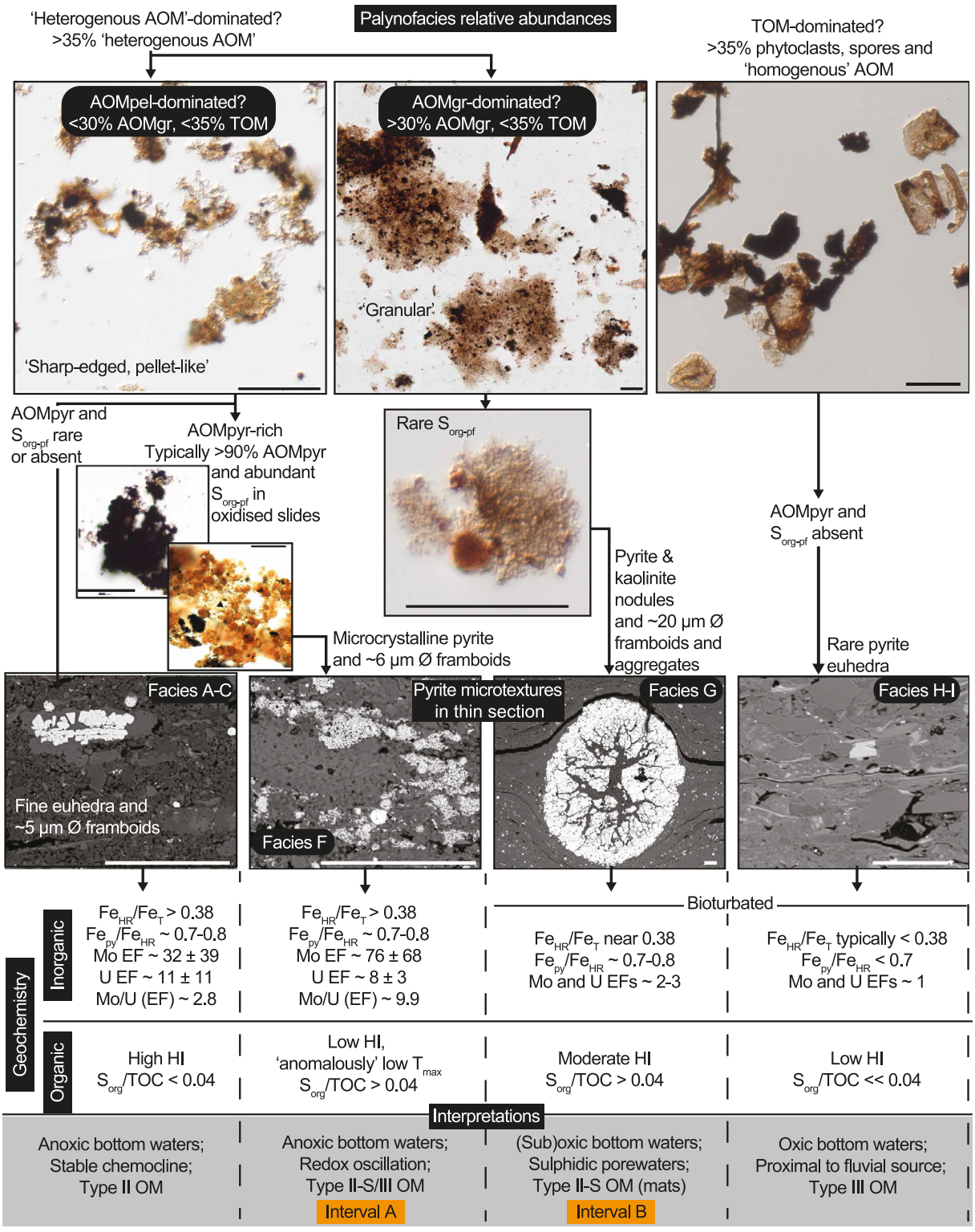

Fig. 10. Summary of key observations and interpretations spanning palynology and organic geochemistry (this study) and sedimentology (Emmings et al., 2019). Backscattered electron microphotographs are also reported by Emmings (2018). All scale bars = 50 µm. Generalized geochemistry includes mean Mo and U EFs with uncertainty quantified as two standard deviations.

and pyrite microtextures described by Emmings (2018) and Emmings et al. (2019). A ternary plot of AOMpel + AOMpyr versus AOMgr versus spores + phytoclasts (Fig. 11) links palynofacies abundances to bottom and pore water redox conditions, water column productivity and proximity to fluvial (deltaic) supply of spores and phytoclasts. Field I delineates AOMgr-rich samples located in the paralic Widermerpool Gulf (Hennissen et al., 2017). Field I is a mixing line between AOMgr and spores and phytoclasts. Lack of AOMpel suggests relatively low productivity water column conditions. Dominance of AOMgr in Field I may indicate widespread occurrences of candidate microbial mats existed in these paralic basins, supported by a long-lived, restriction-driven redox gradient near or at seabed. Alternatively, it is possible AOMgr is

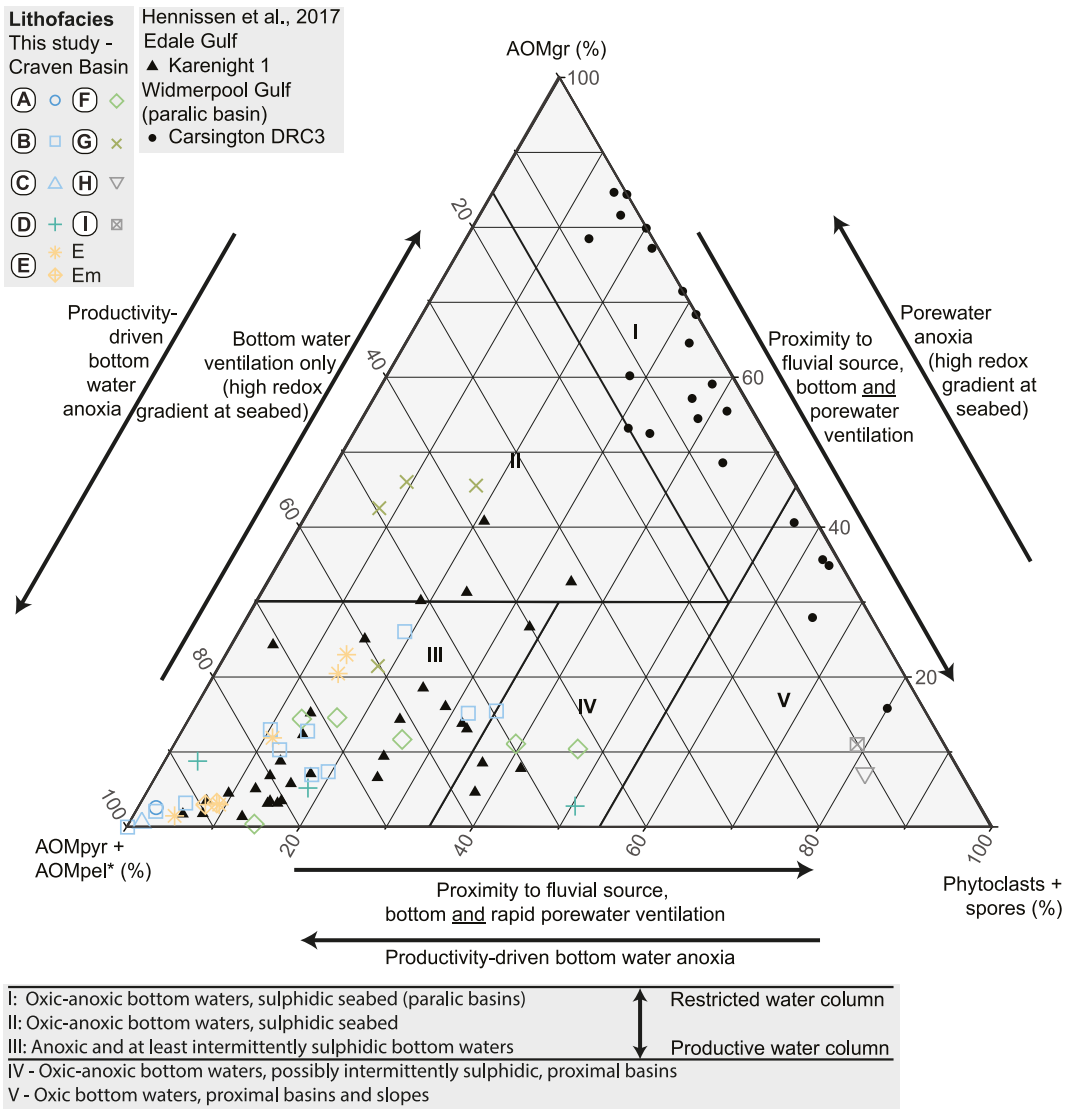

Fig. 11. Ternary plot of AOMpel + AOMpyr versus AOMgr versus spores + phytoclasts. See Fig. 2 and Emmings et al. (2019) for sedimentary facies description. Palynofacies abundance data for the Morridge Formation in the Edale Gulf (borehole Karenight 1) and Widmerpool Gulf (borehole Carsington DRC3), from Hennissen et al. (2017), are also plotted for comparison.

generated via multiple pathways; perhaps AOMgr also includes a component of bacterially modified terrestrial OM (TOM). Field II is interpreted to indicate low to moderate water column productivity, dominantly oxic or suboxic bottom water conditions and sulphidic conditions near or at seabed (Figs. 11, 12a). The atomic S_{org}/TOC in Field II (Interval B) exceeds 0.04 (Table 1; Fig. 12b), the threshold for definition of Type II-S kerogen (Orr, 1986).

Field III represents moderate to high rates of water column productivity and autochthonous OM export to seabed, linked to anoxic and at least intermittently sulphidic bottom water conditions (Figs. 11; 12a). This field includes Type II-S kerogen ($S_{org\text{-}PF}$) generated via early diagenetic redox oscillation (Fig. 9b). $S_{org\text{-}PF}$ exhibits a possible catalytic effect on T_{max} (Lewan, 1998). The majority of Bowland Shale samples from the Craven Basin and contemporaneous mudstones from the Edale Gulf (Hennissen et al., 2017) plot within this field. This suggests productivity was relatively widespread, and perhaps stimulated by nutrient loading from the nearby Pendle delta system (Figs. 1a, 9a–b) (Emmings, 2018). Field V represents oxygenated conditions and/or close proximity to the supply of TOM (Figs. 9, 12a). Facies H–I in Cominco S9, located proximal to the Pendle delta system and deposited during reduced basin accommodation, are sited in this field. Thus Field IV likely represents transitional settings defined by fluctuating oxic/suboxic and anoxic conditions, or significant supply of spores and phytoclasts into anoxic bottom waters (Fig. 11).

The mixing line between fields III and V (and therefore through Field IV; Fig. 11) represents increasing proximity to fluvial sources and/or bottom and pore water ventilation that was sufficiently gradual or diffuse. This inhibited development of a high redox gradient at seabed. Candidate microbial mats (AOMgr) were unable to colonize seabed in these settings. The mixing line between fields III and I represents rapid bottom water ventilation and/or high frequency redox fluctuation, coupled to persistently stagnant or advective, sulphidic porewaters near seabed. This configuration supported colonization by the candidate microbial mats.

Hydrogen index (HI), a key measure for hydrocarbon source rock potential, is highest near Field I and III apices for all immature to early oil-mature data plotted (Fig. 12c; including data from Hennissen et al., 2017). Absence of inorganic geochemical data for Field I precludes assessment of the mechanism for high HI in this field. However, assuming paralic basins were subject to long-lived and stable redoxclines near seabed, it is plausible these conditions promoted condensation and preservation of relatively labile (aliphatic) OM. High HI in Field III is best explained by enhanced preservation of labile OM under sulphidic bottom water conditions beneath a stable redoxcline.

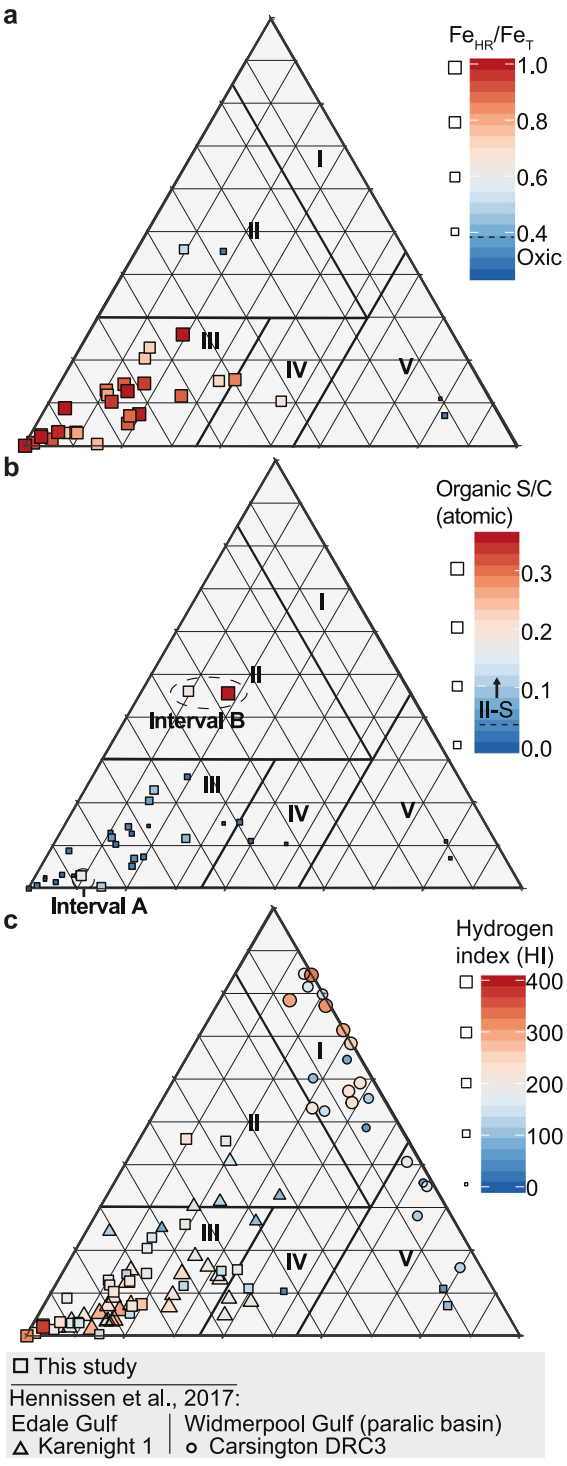

Fig. 12. Ternary plot of AOMpel + AOMpyr versus AOMgr versus spores + phytoclasts (see Fig. 11 for details), with (a) Fe_{HR}/Fe_T; (b) organic S/C, and; (c) hydrogen index (HI) mapped to each data point. Palynofacies abundance data for the Morridge Formation in the Edale Gulf (borehole Karenight 1) and Widmerpool Gulf (borehole Carsington DRC3), from Hennissen et al. (2017), are also plotted with HI. See text for discussion.

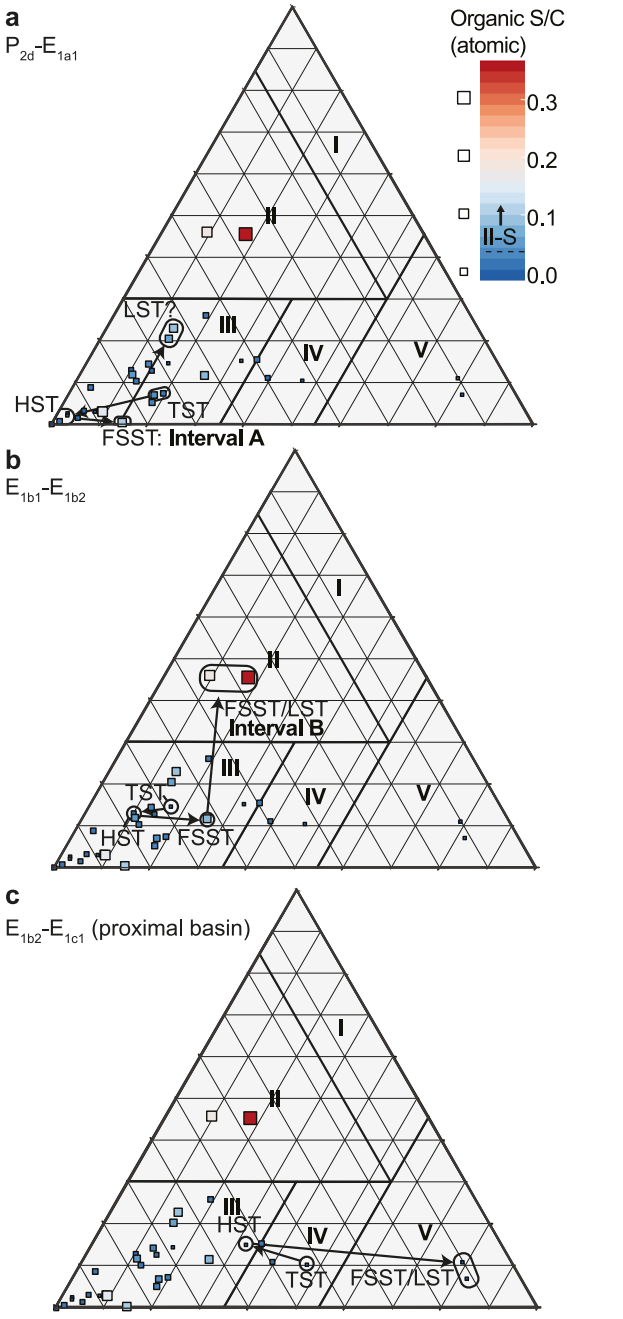

Fig. 13. Ternary plot of AOMpel + AOMpyr versus AOMgr versus spores + phytoclasts (see Fig. 11 for details), with organic S/C mapped to each data point and interpreted basin accommodation pathways from Emmings et al. (2019). Basin accommodation pathways are at least partially equivalent to the eustatic sea level systems tracts of Posamentier et al. (1988). TST = transgressive systems tract; HST = highstand systems tract; FSST = falling stage systems tract; LST = lowstand systems tract.

Changing basin accommodation during deposition of the Bowland Shale is considered at least partially equivalent to eustatic sea level systems tracts (Posamentier et al., 1988). A sequence-stratigraphic control on OM type is important for understanding the link between source rock heterogeneity and timing of hydrocarbon generation and expulsion from this source rock. The effect of changing sea level for biozones E_{1a1} to E_{1c1} is summarized using the ternary plot of AOMpel + AOMpyr versus AOMgr versus spores + phytoclasts (Fig. 13). Key intervals deposited during falling sea level contain bulk Type II-S OM, which likely entered the oil window at a relatively low temperature (e.g., Dembicki, 2009). Understanding the distribution and type of OM is important for exploring this unconventional hydrocarbon resource in the UK (e.g., Andrews, 2013; Clarke et al., 2018), especially if Type II-S intervals are laterally extensive. The possibility that sulphide-oxidizing microbial mats colonized seabed, and across several basins, suggests nutrient and inorganic S and C cycling in epicontinental Mississisippian seaways likely operated in a vastly different way compared to modern oceans.

5. Conclusions

Geochemical and palynological data were integrated through the Upper Bowland Shale unit in the Craven Basin (Lancashire, UK), a basin with ongoing hydrocarbon exploration. Fe-speciation, trace element geochemistry and $\delta^{34}S_{py}$ analyses were utilized in order to assess syngenetic and early diagenetic redox conditions. These data were integrated with sedimentological and palynological observations, in order to understand the controls on OM sulphurization and the distribution of AOM.

Particulate OM in the Upper Bowland Shale is dominated by two types of AOM; "homogenous" AOM (AOMpel) and "heterogeneous, granular" AOM (AOMgr). On the basis of textural observations, AOMpel most likely represent the fecal minipellets of zooplankton and/or pellets of macro-zooplankters. On the transition from anoxic to oxic bottom waters, AOMgr replaces AOMpel as the dominant type of AOM (Interval B). A large particle diameter (likely >500 μm), sheet-like, fragmented character, and presence of candidate organic sheaths suggests AOMgr at least partially represent fragments of benthic microbial mats, likely as sulphide-oxidizers.

Abundant orange, high-relief organic spheres are recognized within each AOM particle, particularly in one key interval (A) overlying the E_{1a1} marine band. These textures are associated with a high S_{org} content and are therefore interpreted as sulphurized OM local to pyrite framboids ($S_{org\text{-}PF}$). Sulphurization is linked to early diagenetic redox oscillation processes. Whilst the precise mechanism for sulphurization is unclear, we propose redox oscillation promoted sulphurization in two ways. Firstly, redox oscillation enhanced the degradation of OM. This produced organic compounds prone to sulphurization. Secondly, redox oscillation also promoted S cycling across micro-redox fronts local to each framboid. Intermediate, and therefore reactive, S species were thus available for complexation with OM.

$S_{org\text{-}PF}$ formed primarily under anoxic conditions during periods of reduced sea level (Interval A), via an increased supply of Fe_{HR} from adjacent shelves. An increased supply of Fe_{HR} stimulated redox oscillation between ferruginous and euxinic conditions, which promoted acidification of porewaters near seabed. Redox oscillation was associated with S cycling required to generate reactive S species.

Both intervals A and B exhibit $S_{org}/TOC > 0.04$ and are therefore interpreted as Type II-S kerogen. A ternary plot of AOMpel + AOMpyr versus AOMgr versus spores + phytoclasts links the observed palynofacies and sulphurization (intervals A and B) to bottom and pore water redox conditions, water column productivity and proximity to fluvial (deltaic) supply of spores and phytoclasts. These variables were moderated by changing basin accommodation, driven primarily by eustatic sea level fluctuation. This is important for understanding the link between source rock heterogeneity and timing of hydrocarbon generation and expulsion from this source rock.

Acknowledgements

This study was funded by the Natural Environment Research Council (NERC), [grant no. NE/L002493/1], within the Central England Training Alliance (CENTA). The study also received CASE funding from the British Geological Survey. SWP acknowledges support from a Royal Society Wolfson Research Merit Award. Nick Riley (Carboniferous Ltd) is thanked for sharing biostratigraphic expertise and assistance. Nick Marsh and Tom Knott are thanked for providing assistance during geochemical analyses. Jane Flint is thanked for preparation of the palynological slides. BGS authors publish with the approval of the Executive Director of the British Geological Survey.

Appendix A. Supplementary data

Supplementary data to this article can be found online at https://doi.org/10.1016/j.revpalbo.2019.04.004.

References

Adam, P., Schneckenburger, P., Schaeffer, P., Albrecht, P., 2000. Clues to early diagenetic sulfurization processes from mild chemical cleavage of labile sulfur-rich geomacromolecules. Geochim. Cosmochim. Acta 64 (20), 3485–3503.
Aitkenhead, N., Bridge, D., Riley, N.J., Kimbell, S., 1992. Geology of the Country around Garstang: Memoir for 1:50 000 Sheet 67. HMSO, London.
Aizenshtat, Z., Krein, E.B., Vairavamurthy, M.A., Goldstein, T.P., 1995. Role of Sulfur in the Transformations of Sedimentary Organic Matter: A Mechanistic Overview, Geochemical Transformations of Sedimentary Sulfur. ACS Symposium SeriesAmerican Chemical Society, pp. 16–37.
Algeo, T.J., Tribovillard, N., 2009. Environmental analysis of paleoceanographic systems based on molybdenum–uranium covariation. Chem. Geol. 268 (3–4), 211–225.
Aller, R.C., 1982. Carbonate dissolution in nearshore terrigenous muds: the role of physical and biological reworking. J. Geol. 90 (1), 79–95.
Aller, R.C., 1998. Mobile deltaic and continental shelf muds as suboxic, fluidized bed reactors. Mar. Chem. 61 (3), 143–155.
Amrani, A., 2014. Organosulfur compounds: molecular and isotopic evolution from biota to oil and gas. Annu. Rev. Earth Planet. Sci. 42 (1), 733–768.
Amrani, A., Aizenshtat, Z., 2004. Mechanisms of sulfur introduction chemically controlled: δ34S imprint. Org. Geochem. 35 (11), 1319–1336.
Andrews, I.J., 2013. The Carboniferous Bowland Shale Gas Study: Geology and Resource Estimation. British Geological Survey for Department of Energy and Climate Change.
Aplin, A.C., Macquaker, J.H.S., 1993. Quantifying sedimentary geochemical processes - C-S-Fe geochemistry of some modern and ancient anoxic marine muds and mudstones. Phil. Trans. R. Soc. Lond. Ser. A: Phys. Eng. Sci. 344 (1670), 89–100.
Arthurton, R.S., 1984. The Ribblesdale fold belt, NW England—a Dinantian-early Namurian dextral shear zone. Geol. Soc. Lond., Spec. Publ. 14 (1), 131–138.
Aycard, M., et al., 2003. Formation pathways of proto-kerogens in Holocene sediments of the upwelling influenced Cariaco Trench, Venezuela. Org. Geochem. 34 (6), 701–718.
Bailey, J.V., Orphan, V.J., Joye, S.B., Corsetti, F.A., 2009. Chemotrophic microbial mats and their potential for preservation in the rock record. Astrobiology 9 (9), 843–859.
Beaumont, K.L., Nash, G.V., Davidson, A.T., 2002. Ultrastructure, morphology and flux of microzooplankton faecal pellets in an East Antarctic fjord. Mar. Ecol. Prog. Ser. 245, 133–148.
Bisat, W.S., 1923. The carboniferous goniatites of the north of England and their zones. Proc. Yorks. Geol. Soc. 20 (1), 40–124.
Brandon, A., et al., 1998. Geology of the Country around Lancaster: Memoir for 1:50 000 Sheet 59. The Stationary Office, London.
Bruland, K.W., Silver, M.W., 1981. Sinking rates of fecal pellets from gelatinous zooplankton (Salps, Pteropods, Doliolids). Mar. Biol. 63 (3), 295–300.
Burdige, D.J., 2006. Geochemistry of Marine Sediments. Princeton University Press, USA.
Canfield, D.E., Teske, A., 1996. Late Proterozoic rise in atmospheric oxygen concentration inferred from phylogenetic and sulphur-isotope studies. Nature 382, 127.
Canfield, D.E., Raiswell, R., Westrich, J.T., Reaves, C.M., Berner, R.A., 1986. The use of chromium reduction in the analysis of reduced inorganic sulfur in sediments and shales. Chem. Geol. 54 (1), 149–155.
Canfield, D.E., Raiswell, R., Bottrell, S.H., 1992. The reactivity of sedimentary iron minerals toward sulfide. Am. J. Sci. 292 (9), 659–683.
Canfield, D.E., Farquhar, J., Zerkle, A.L., 2010. High isotope fractionations during sulfate reduction in a low-sulfate euxinic ocean analog. Geology 38 (5), 415–418.
Catuneanu, O., 2007. Sequence stratigraphic context of microbial mat features. In: Schieber, J., et al. (Eds.), Atlas of microbial mat features preserved within the clastic rock record. Elsevier, pp. 276–283.
Clarke, H., Turner, P., Bustin, R.M., Riley, N., Besly, B., 2018. Shale gas resources of the Bowland Basin, NW England: a holistic study. Pet. Geosci. 24 (3), 287–322.
Cuomo, M.C., Chen, Y.Y., 1996. Pellets and epifluorescence. In: Jansonius, J., McGregor, D. (Eds.), Palynology: Principles and Applications. 1. American Association of Stratigraphic Palynologists Foundation, pp. 1092–1097.
Davies, S.J., 2008. The record of Carboniferous sea-level change in low-latitude sedimentary successions from Britain and Ireland during the onset of the late Paleozoic ice age. Geol. Soc. Am. Spec. Pap. 441, 187–204.
Davies, R.J., Austin, R., Moore, D., 1993. Environmental controls of Brigantian conodont-distribution: evidence from the Gayle limestone of the Yoredale Group in Northern England. Ann. Soc. Géol. Belgique 116, 221–241 (Fascicule 2 - Carboniferous biostratigraphy).
Davies, S., Hampson, G., Flint, S., Elliott, T., 1999. Continental-scale sequence stratigraphy of the Namurian, Upper Carboniferous and its applications to reservoir prediction. Geol. Soc., Lond., Petrol. Geol. Conf. Ser. 5, 757–770.
Davydov, V.I., Korn, D., Schmitz, M., 2012. The Carboniferous Period. Geologic Time Scale 2012 2-Volume Set. Elsevier.
Dembicki, H., 2009. Three common source rock evaluation errors made by geologists during prospect or play appraisals. AAPG Bull. 93 (3), 341–356.
Earp, J.R., 1961. Geology of the Country around Clitheroe and Nelson (One-Inch Geological Sheet 68, New Series). H.M.S.O.
Eglinton, T.I., Sinninghe Damsté, J.S., Kohnen, M.E.L., de Leeuw, J.W., 1990. Rapid estimation of the organic sulphur content of kerogens, coals and asphaltenes by pyrolysis-gas chromatography. Fuel 69 (11), 1394–1404.
Emmings, J., 2018. Controls on UK Lower Namurian Shale Gas Prospectivity: Understanding the Spatial and Temporal Distribution of Organic Matter in Siliciclastic Mudstones. PhD Thesis. University of Leicester.
Emmings, J., et al., 2017. Stream and slope weathering effects on organic-rich mudstone geochemistry and implications for hydrocarbon source rock assessment: a Bowland Shale case study. Chem. Geol. 471, 74–91.
Emmings, J., et al., 2019. From marine bands to hybrid flows: sedimentology of a Mississippian Black Shale. Sedimentology Accepted Manuscript.

Espitalie, J., Madec, M., Tissot, B., Mennig, J.J., Leplat, P., 1977. Source Rock Characterization Method for Petroleum Exploration. Offshore Technology Conference.

Filley, T.R., Freeman, K.H., Wilkin, R.T., Hatcher, P.G., 2002. Biogeochemical controls on reaction of sedimentary organic matter and aqueous sulfides in holocene sediments of Mud Lake, Florida. Geochim. Cosmochim. Acta 66 (6), 937–954.

Fossing, H., et al., 1995. Concentration and transport of nitrate by the mat-forming sulphur bacterium *Thioploca*. Nature 374, 713.

Fraser, A.J., Gawthorpe, R.L., 1990. Tectono-stratigraphic development and hydrocarbon habitat of the Carboniferous in northern England. Geol. Soc. Lond. Sp. Publ. 55 (1), 49–86.

Gastaldo, R.A., Purkyňová, E., Šimůnek, Z., Schmitz, M.D., 2009. Ecological persistence in the Late Mississippian (Serpukhovian, Namurian A) megafloral record of the Upper Silesian Basin, Czech Republic. Palaios 24 (6), 336–350.

Gawthorpe, R., 1987. Tectono-sedimentary evolution of the Bowland Basin, N England, during the Dinantian. J. Geol. Soc. 144, 59–71.

Gowing, M.M., Silver, M.W., 1985. Minipellets: a new and abundant size class of marine fecal pellets. J. Mar. Res. 43 (2), 395–418.

Grant, C.W., 1991. Lateral and vertical distributions and textural features of filamentous bacterial (*Beggiatoa* sp.) mats in Santa Barbara basin, California. AAPG Bulletin Annual meeting of the American Association of Petroleum Geologists (AAPG), Dallas, TX (United States), 7–10 Apr 1991 None, pp. Medium: X; Size: Pages: 585.

Grossi, V., et al., 1998. Biotransformation pathways of phytol in recent anoxic sediments. Org. Geochem. 29 (4), 845–861.

Grunke, S., et al., 2011. Niche differentiation among mat-forming, sulfide-oxidizing bacteria at cold seeps of the Nile Deep Sea Fan (Eastern Mediterranean Sea). Geobiology 9 (4), 330–348.

Hartgers, W.A., et al., 1997. Sulfur-binding in recent environments: II. Speciation of sulfur and iron and implications for the occurrence of organo-sulfur compounds. Geochim. Cosmochim. Acta 61 (22), 4769–4788.

Hennissen, J.A.I., et al., 2017. The prospectivity of a potential shale gas play: an example from the southern Pennine Basin (Central England, UK). Mar. Pet. Geol. 86, 1047–1066.

Henschke, N., Everett, J.D., Richardson, A.J., Suthers, I.M., 2016. Rethinking the role of salps in the ocean. Trends Ecol. Evol. 31 (9), 720–733.

Holdsworth, B., Collinson, J.D., 1988. Millstone Grit cyclicity revisited. In: Besly, B.M., Kelling, G. (Eds.), Sedimentation in a Synorogenic Basin Complex: The Upper Carboniferous of Northwest Europe. Blackie, Glasgow, pp. 132–152.

Jarvie, D.M., 2012. Shale resource systems for oil and gas: part 1 - Shale-gas resource systems. Shale reservoirs - Giant resources for the 21st century: AAPG Memoir 97.

Kampschulte, A., Bruckschen, P., Strauss, H., 2001. The sulphur isotopic composition of trace sulphates in carboniferous brachiopods: implications for coeval seawater, correlation with other geochemical cycles and isotope stratigraphy. Chem. Geol. 175 (1), 149–173.

Kane, I.A., 2010. Development and flow structures of sand injectities: the Hind Sandstone Member injectite complex, Carboniferous, UK. Mar. Pet. Geol. 27, 1200–1215.

Kerschke, D., Schulz, H.-M., 2013. The shale gas potential of Tournaisian, Visean, and Namurian black shales in North Germany: baseline parameters in a geological context. Environ. Earth Sci. 70 (8), 3817–3837.

Kirby, G.A., et al., 2000. Structure and evolution of the Craven Basin and adjacent areas. Subsurface Memoir of the British Geological Survey.

Könitzer, S.F., Stephenson, M.H., Davies, S.J., Vane, C.H., Leng, M.J., 2016. Significance of sedimentary organic matter input for shale gas generation potential of Mississippian Mudstones, Widmerpool Gulf, UK. Review of Palaeobotany and Palynology 224 (Part 2), 146–168.

Lampitt, R.S., Salter, I., Johns, D., 2009. Radiolaria: Major exporters of organic carbon to the deep ocean. Global Biogeochemical Cycles 23 (1).

Leeder, M.R., 1982. Upper Palaeozoic basins of the British Isles—Caledonide inheritance versus Hercynian plate margin processes. J. Geol. Soc. 139 (4), 479–491.

Lewan, M.D., 1984. Factors controlling the proportionality of vanadium to nickel in crude oils. Geochim. Cosmochim. Acta 48 (11), 2231–2238.

Lewan, M.D., 1998. Sulphur-radical control on petroleum formation rates. Nature 391 (6663), 164–166.

Lin, R., Davis, A., 1988. The Chemistry of Coal Maceral Fluorescence with Special Reference to the Huminite/Vitrinite Group, Energy and Fuels Research Center. College of Earth and Mineral Sciences, The Pennsylvania State University.

Love, L.G., 1957. Micro-organisms and the presence of syngenetic pyrite. Quart. J. Geol. Soc. 113 (1–4), 429–436 NP, 437–440.

Love, L.G., 1962. Further studies on micro-organisms and the presence of syngenetic pyrite. Palaeontology 5.

Lyons, T.W., Severmann, S., 2006. A critical look at iron paleoredox proxies: New insights from modern euxinic marine basins. Geochim. Cosmochim. Acta 70 (23), 5698–5722.

Ma, K., Schicho, R.N., Kelly, R.M., Adams, M.W., 1993. Hydrogenase of the hyperthermophile *Pyrococcus furiosus* is an elemental sulfur reductase or sulfhydrogenase: evidence for a sulfur-reducing hydrogenase ancestor. Proc. Natl. Acad. Sci. 90 (11), 5341–5344.

Ma, K., Weiss, R., Adams, M.W.W., 2000. Characterization of Hydrogenase II from the Hyperthermophilic Archaeon Pyrococcus furiosus and Assessment of Its Role in Sulfur Reduction. J. Bacterio. 182 (7), 1864–1871.

MacLean, L.C., et al., 2008. A high-resolution chemical and structural study of framboidal pyrite formed within a low-temperature bacterial biofilm. Geobiology 6 (5), 471–480.

Maher, L.J., 1981. Statistics for microfossil concentration measurements employing samples spiked with marker grains. Rev. Palaeobot. Palynol. 32 (2), 153–191.

Martinsen, O.J., Collinson, J.D., Holdsworth, B.K., 1995. Millstone Grit Cyclicity Revisited, II: Sequence Stratigraphy and Sedimentary Responses to Changes of Relative Sea-Level, Sedimentary Facies Analysis. Blackwell Publishing Ltd., pp. 305–327.

Menning, M., et al., 2006. Global time scale and regional stratigraphic reference scales of Central and West Europe, East Europe, Tethys, South China, and North America as used in the Devonian–Carboniferous–Permian Correlation Chart 2003 (DCP 2003). Palaeogeogr. Palaeoclimatol. Palaeoecol. 240 (1–2), 318–372.

Moseley, F., 1952. The Namurian of the Lancaster Fells. Quart. J. Geol. Soc. 109 (1–4), 423–450 NP, 451–454.

Moseley, F., 1962. The structure of the south-western part of the Sykes Anticline, Bowland, West Yorkshire. Proc. York. Geol. Polytechn. Soc. 33 (3), 287–314.

Mossmann, J.-R., Aplin, A.C., Curtis, C.D., Coleman, M.L., 1991. Geochemistry of inorganic and organic sulphur in organic-rich sediments from the Peru Margin. Geochim. Cosmochim. Acta 55 (12), 3581–3595.

Nissenbaum, A., Presley, B.J., Kaplan, I.R., 1972. Early diagenesis in a reducing fjord, Saanich Inlet, British Columbia—I. chemical and isotopic changes in major components of interstitial water. Geochim. Cosmochim. Acta 36 (9), 1007–1027.

Nyhuis, C.J., Riley, D., Kalasinska, A., 2015. Thin section petrography and chemostratigraphy: Integrated evaluation of an upper Mississippian mudstone dominated succession from the southern Netherlands. Netherl. J. Geosci. Geol. Mijnbouw 95 (1), 3–22.

Ohfuji, H., Rickard, D., 2005. Experimental syntheses of framboids—a review. Earth Sci. Rev. 71 (3–4), 147–170.

Orr, W., 1986. Kerogen/asphaltene/sulfur relationships in sulfur-rich monterey oils. Adv. Org. Geochem. 10, 499–516.

Pacton, M., Fiet, N., Gorin, G.E., 2007. Bacterial activity and preservation of sedimentary organic matter: the role of exopolymeric substances. Geomicrobiol J. 24 (7–8), 571–581.

Pacton, M., Gorin, G.E., Vasconcelos, C., 2011. Amorphous organic matter — experimental data on formation and the role of microbes. Rev. Palaeobot. Palynol. 166 (3–4), 253–267.

Pitrat, C.W., 1970. Phytoplankton and the late Paleozoic wave of extinction. Palaeogeogr. Palaeoclimatol. Palaeoecol. 8 (1), 49–54.

Porter, K.G., Robbins, E.I., 1981. Zooplankton fecal pellets link fossil fuel and phosphate deposits. Science 212 (4497), 931–933.

Posamentier, H.W., Jervey, M.T., Vail, P.R., 1988. Eustatic controls on clastic deposition i - conceptual framework. SEPM Spec. Publ. 42.

Poulton, S.W., Canfield, D.E., 2005. Development of a sequential extraction procedure for iron: implications for iron partitioning in continentally derived particulates. Chem. Geol. 214 (3), 209–221.

Poulton, S.W., Canfield, D.E., 2011. Ferruginous conditions: a dominant feature of the ocean through earth's history. Elements 7 (2), 107–112.

Poulton, S.W., Raiswell, R., 2002. The low-temperature geochemical cycle of iron: from continental fluxes to marine sediment deposition. Am. J. Sci. 302 (9), 774–805.

Raiswell, R., Canfield, D., 1998. Sources of iron for pyrite formation in marine sediments. Am. J. Sci. 298 (3), 219–245.

Ramsbottom, W.H.C., 1973. Transgressions And Regressions In The Dinantian: A New Synthesis Of British Dinantian Stratigraphy. Proc. Yorks. Geol. Polytech. Soc. 39 (4), 567–607.

Ramsbottom, W.H.C., 1977. Major cycles of transgression and regression (mesothems) in the Namurian. Proc. Yorks. Geol. Polytech. Soc. 41 (3), 261–291.

Ramsbottom, W.H.C., Saunders, W.B., 1985. Evolution and evolutionary biostratigraphy of carboniferous ammonoids. J. Paleontol. 59 (1), 123–139.

Rickard, D., 2012. Chapter 6 - Sedimentary Pyrite. In: David, R. (Ed.), Developments in Sedimentology. Elsevier, pp. 233–285.

Riegel, W., 1996. The geologic significance of the Late Paleozoic phytoplankton blackout. IX IPC Meeting, Houston, Texas, USA abstracts, pp. 133–134.

Riegel, W., 2008. The Late Palaeozoic phytoplankton blackout — Artefact or evidence of global change? Rev. Palaeobot. Palynol. 148 (2), 73–90.

Riley, N., et al., 1993. Geochronometry and geochemistry of the European mid-Carboniferous boundary global stratotype proposal, Stonehead Beck, North Yorkshire, UK. Ann. Soc. Geol. Belgique, T 116 (fascicule 2), 275–289.

Rontani, J.-F., Bonin, P.C., Volkman, J.K., 1999. Biodegradation of free phytol by bacterial communities isolated from marine sediments under aerobic and denitrifying conditions. Appl. Environ. Microbiol. 65 (12), 5484–5492.

Schieber, J., 1986. The possible role of benthic microbial mats during the formation of carbonaceous shales in shallow Mid-Proterozoic basins. Sedimentology 33 (4), 521–536.

Schieber, J., Sur, S., Banerjee, S., 2007a. Benthic microbial mats in black shale units from the Vindhyan Supergroup, Middle Proterozoic of India: the challenges of recognizing the genuine article. In: Schieber, J., et al. (Eds.), Atlas of microbial mat features preserved within the clastic rock record. Elsevier, pp. 189–197.

Schieber, J., Sur, S., Banerjee, S., 2007b. Microbial mats on muddy substrates - examples of possible sedimentary features and underlying processes. In: Schieber, J., et al. (Eds.), Atlas of microbial mat features preserved within the clastic rock record. Elsevier, pp. 189–197.

Schindelin, J., et al., 2012. Fiji: an open-source platform for biological-image analysis. Nat. Methods 9, 676.

Seckbach, J., Oren, A., 2010. Microbial mats: modern and ancient microorganisms in stratified systems. Cellular Origin, Life in Extreme Habitats and Astrobiology. 14.

Servais, T., Martin, R.E., Nützel, A., 2016. The impact of the 'terrestrialisation process' in the late Palaeozoic: pCO2, pO2, and the 'phytoplankton blackout'. Rev. Palaeobot. Palynol. 224 (Part 1), 26–37.

Sholkovitz, E.R., Price, N.B., 1980. The major-element chemistry of suspended matter in the Amazon Estuary. Geochim. Cosmochim. Acta 44 (2), 163–171.

Sievert, S.M., Wieringa, E.B., Wirsen, C.O., Taylor, C.D., 2007. Growth and mechanism of filamentous-sulfur formation by Candidatus *Arcobacter sulfidicus* in opposing oxygen-sulfide gradients. Environ. Microbiol. 9 (1), 271–276.

Sinninghe Damsté, J.S., De Leeuw, J.W., 1990a. Analysis, structure and geochemical significance of organically-bound sulphur in the geosphere: state of the art and future research. Adv. Org. Geochem. 16 (4–6), 1077–1101.

Sinninghe Damsté, J.S., De Leeuw, J.W., 1990b. Organic sulfur compounds and other biomarkers as indicators of palaeosalinity. In: Orr, W., White, W. (Eds.), Geochemistry of Sulfur in Fossil Fuels. American Chemical Society.
Sinninghe Damsté, J.S., Eglinton, T.I., De Leeuw, J.W., Schenck, P.A., 1989. Organic sulphur in macromolecular sedimentary organic matter: I. Structure and origin of sulphur-containing moieties in kerogen, asphaltenes and coal as revealed by flash pyrolysis. Geochim. Cosmochim. Acta 53 (4), 873–889.
Słowakiewicz, M., et al., 2015. Shale-gas potential of the mid-carboniferous Bowland-Hodder Unit in the Cleveland Basin (Yorkshire), Central Britain. J. Pet. Geol. 38 (1), 59–75.
Soetaert, K., Hofmann, A.F., Middelburg, J.J., Meysman, F.J.R., Greenwood, J., 2007. The effect of biogeochemical processes on pH. Mar. Chem. 105 (1), 30–51.
Steudel, R., 1989. On the nature of the "elemental sulfur" (S^0) produced by sulfur-oxidising bacteria - a model for S^0 globules. In: Schlegel, H., Bowien, B. (Eds.), Biological of Autotrophic Bacteria. Science Technology Publishing, Madison, USA.
Stockmarr, J., 1971. Tablets with spores used in absolute pollen analysis. Pollen et spores, XIII 4.
Stoecker, D.K., 1984. Particle production by planktonic ciliates. Limnol. Oceanogr. 29 (5), 930–940.
Tappan, H., 1970. Phytoplankton abundance and Late Paleozoic extinctions: a reply. Palaeogeogr. Palaeoclimatol. Palaeoecol. 8 (1), 56–66.
Taylor, S., McLennan, S., 1985. The Continental Crust: Its Composition and Evolution. Blackwell Scientific, London, p. 312.
Tribovillard, N., Trentesaux, A., Trichet, J., Défarge, C., 2000. A Jurassic counterpart for modern kopara of the Pacific atolls: lagoonal, organic matter-rich, laminated carbonate of Orbagnoux (Jura Mountains, France). Palaeogeogr. Palaeoclimatol. Palaeoecol. 156 (3), 277–288.
Tribovillard, N., Bialkowski, A., Tyson, R.V., Lallier-Vergès, E., Deconinck, J.F., 2001. Organic facies variation in the late Kimmeridgian of the Boulonnais area (northernmost France). Mar. Pet. Geol. 18 (3), 371–389.
Tribovillard, N., Algeo, T., Lyons, T., Ruboulleau, A., 2006. Trace metals as paleoredox and paleoproductivity proxies: an update. Chem. Geol. 232, 12–32.
Tyson, R., 1989. Late Jurassic palynofacies trends, Piper and Kimmeridge Clay Formations, UK onshore and offshire. In: Batter, D., Keen, M. (Eds.), Northwest European Micropalaeontology and Palynology. British Micropalaeontological Society Series. Ellis Horwood, Chichester, pp. 135–172.
Tyson, R., 1995. Sedimentary Organic Matter: Organic Facies and Palynofacies London.
Van Kaam-Peters, H.M.E., Schouten, S., Köster, J., Sinninghe Damstè, J.S., 1998. Controls on the molecular and carbon isotopic composition of organic matter deposited in a Kimmeridgian euxinic shelf sea: evidence for preservation of carbohydrates through sulfurisation. Geochim. Cosmochim. Acta 62 (19), 3259–3283.
Veevers, J.J., Powell, C.M., 1987. Late Paleozoic glacial episodes in Gondwanaland reflected in transgressive-regressive depositional sequences in Euramerica. Geol. Soc. Am. Bull. 98 (4), 475–487.
Wang, F., Chapman, P.M., 1999. Biological implications of sulfide in sediment—a review focusing on sediment toxicity. Environ. Toxicol. Chem. 18 (11), 2526–2532.
Warr, L.N., 2000. The Variscan Orogeny: the welding of Pangaea. In: Woodcock, N.H., Strachan, R. (Eds.), Geological History of Britain and Ireland. Wiley-Blackwell, Hoboken, USA, pp. 271–294.
Wasmund, K., Mußmann, M., Loy, A., 2017. The life sulfuric: microbial ecology of sulfur cycling in marine sediments. Environ. Microbiol. Rep. 9 (4), 323–344.
Waters, C.N., Condon, D.J., 2012. Nature and timing of Late Mississippian to Mid-Pennsylvanian glacio-eustatic sea-level changes of the Pennine Basin, UK. J. Geol. Soc. 169 (1), 37–51.
Waters, C.N., Davies, S.J., 2006. Carboniferous: extensional basins, advancing deltas and coal swamps. In: Brenchley, P.J. (Ed.), The Geology of England and Wales. Geological Society of London, London, England, pp. 173–223.
Waters, C.N., Browne, M.A.E., Dean, M.T., Powell, J.H., 2007. Lithostratigraphical framework for Carboniferous successions of Great Britain (Onshore). British Geological Survey Research Report, RR/07/01.
Waters, C.N., Waters, R.A., Barclay, W.J., Davies, J.R., 2009. A lithostratigraphical framework for the Carboniferous successions of southern Great Britain (onshore). British Geological Survey Research Report, RR/09/01.
Wignall, P.B., Newton, R., 1998. Pyrite framboid diameter as a measure of oxygen deficiency in ancient mudrocks. Am. J. Sci. 298 (7), 537–552.
Williams, L.A., 1984. Subtidal stromatolites in Monterey Formation and other organic-rich rocks as suggested source contributors to petroleum formation. AAPG Bull. 68 (12), 1879–1893.
Wirsen, C.O., et al., 2002. Characterization of an autotrophic sulfide-oxidizing marine Arcobacter sp. that produces filamentous sulfur. Appl. Environ. Microbiol. 68 (1), 316–325.
Wood, G.D., Gabriel, A.M., Lawson, J.C., 1996. Palynological techniques - processing and microscopy. In: Jansonius, J., McGregor, D. (Eds.), Palynology: Principles and Applications. 1. American Association of Stratigraphic Palynologists Foundation, pp. 29–50.